Hurricane-like Vortices in Conditionally Unstable Moist Convection

Mu-Hua Chien [1], Olivier M. Pauluis [1,2], Ann S. Almgren [3]

[1]Center for Atmosphere and Ocean Science, New York University, New York, New York
[2]Center for Prototype Climate Modeling, New York University Abu Dhabi, Abu Dhabi, United Arab Emirates
[3]Center for Computational Sciences and Engineering, Lawrence Berkeley National Laboratory, Berkeley, California

Key Points:

- The impact of rotation on simulations of idealized simulations of moist convection is studied;
- For intermediate values of the rotation rate, the flow is dominated by coherent hurricanes-like vortices;
- The presence of coherent vortices enhances the upward heat transport when compared to non-rotating simulations.

Corresponding author: Mu-Hua Chien, `mhc431@nyu.edu`

Abstract

This study investigates the emergence of hurricane-like vortices in idealized simulations of rotating moist convection. A Boussinesq atmosphere with simplified thermodynamics for phase transitions is forced by prescribing the temperature and humidity at the upper and lower boundaries. The governing equations are solved numerically using a variable-density incompressible Navier-Stokes solver with adaptive mesh refinement to explore the behavior of moist convection under a broad range of conditions.

In the absence of rotation, convection aggregates into active patches separated by large unsaturated regions. Rotation modulates this statistical equilibrium state so that the self-aggregated convection organizes hurricane-like vortices. The warm and saturated air converges to the center of the vortices, and the latent heat released through the upwelling forms the warm core structure. These hurricane-like vortices share characteristics similar to tropical cyclones in the earth's atmosphere.

The hurricane-like vortices occur under conditionally unstable conditions where the potential energy given at the boundaries is large enough, corresponding to a moderate rate of rotation. This regime shares many similar characteristics to the tropical atmosphere indicating that the formation of intense meso-scale vortices is a general characteristics of rotating moist convection. The model used here does no include any interactions with radiation, wind-evaporation feedback, or cloud microphysics, indicating that, while these processes may be relevant for tropical cyclogenesis in the Earth atmosphere, they are not its primary cause. Instead, our results confirm that the formation and maintenance of hurricane-like vortices involve a combination of atmospheric dynamics under the presence of rotation and of phase transitions.

Plain Language Summary

We apply a numerical simulation of an idealized atmosphere system to investigate the emergence of hurricane-like vortices. The complicated thermodynamics for water vapor is simplified. The remaining system can still produce a conditionally unstable atmosphere in which unsaturated air parcels experience a stable stratification, and unsaturated parcels experience an unstable one. We find self-aggregated convection in the absence of rotation and hurricane-like vortices in the presence of rotation. The warm and saturated air converges to the center of the vortices, and the latent heat released through the upwelling forms the warm core structure. These hurricane-like vortices share characteristics similar to tropical cyclones in the earth's atmosphere. This idealized configuration produces characteristics similar to the tropical atmosphere so that the hurricane-like vortices can be considered as the outcome of the tropical cyclogenesis. However, the tropical cyclogenesis here does not require any interactions with radiation, surface flux feedback, or precipitation. Our results confirm that the formation and maintenance of hurricane-like vortices involve a combination of rotation and a thermodynamic forcing.

1 Introduction

Intense winds in hurricanes and typhoons require the continuous generation of kinetic energy within the storm to balance its loss to frictional dissipation. This occurs as hurricane acts as a heat engine by transporting the energy received from the warm ocean to the colder atmosphere. Fully developed hurricanes in the quasi-steady state can be approximated as axisymmetric vortices in which the flow follows the constant angular momentum lines along the constant entropy surface (Emanuel, 1986). In doing so, it acts as a heat engine that produces the kinetic energy necessary to sustain the storm and transports the heat. This study aims to investigate the mechanism by which these coherent vortices transport heat from a warm bottom surface to a cold top surface in the quasi-equilibrium atmosphere using a simplified model.

Convection compensates for the temperature imbalance triggered by surface heating and radiative cooling to form the statistical equilibrium regime in the atmosphere as known as radiative-convective equilibrium(RCE) regime. Numerical models have successfully reproduced key features of convection in the RCE regime (Muller & Held, 2012; Khairoutdinov & Emanuel, 2013). Convective self-aggregation is the spontaneous spatial organization of convection in numerical simulations of radiative–convective equilibrium in the absence of rotation, and the self-aggregation convection turns into organized vortices in the prcesense of rotation (Wing et al., 2016, 2017). Hurricanes can occur under a wide range of conditions and forcing falling well outside the Earth's current climate (Mrowiec et al., 2011; Cronin & Chavas, 2019). Past studies suggest many possibilities for the key criterion for hurricane formation, such as radiative-convective feedback, surface flux feedback, or the latent heat release of water vapor.

The theory for idealized vortices focuses on the eyewall circulation and the upper bound on the hurricane intensity (Emanuel, 1986). Mrowiec et al. (2011) explores the large-scale features of idealized vortices on the polar coordinate and indicates latent heat release may not be required to sustain an idealized vortex. The analysis by Mrowiec et al. (2016) of isentropic circulation in a WRF simulation indicates the importance of secondary circulation. These models are able to reproduce a number of the large-scale features of a mature vortex, and thus offer important insights into the mature hurricanes. The actual behavior of real storms is much more complex owing to a wide range of scales involved. Here, this study tries to answer whether a simpler configuration for moist convection can produce a hurricane-like vortex. If so, then we can compare the parameter space of a vortex in this configuration to the hurricanes and typhoons in the earth's atmosphere.

To study the conditionally unstable atmosphere in the presence of rotation, this study relies on the system of moist Rayleigh-Bénard convection (MRBC) used in Pauluis and Schumacher (2011). An atmospheric layer is represented as a Boussinesq fluid in which the buoyancy is a non-linear function of two prognostic variables. This simplification retains the critical physics of phase transition while avoiding some of the complexities that arise from cloud microphysics (Pauluis & Schumacher, 2010). This equation set is mathematical equivalent to the model used by Bretherton (1987, 1988). In particular, the parameter space of MRBC can be reduced to five non-dimensional numbers. This opens the model for systematic investigation of the parameter space. The MRBC configuration has been used to study the weak nonlinear convective regime (Bretherton, 1987, 1988), the statistical behavior of stratocumulus convection (Pauluis & Schumacher, 2010; Weidauer et al., 2010), the onset of convection at low to intermediate Rayleigh number (Weidauer et al., 2011), and the conditionally unstable turbulent regime (Pauluis & Schumacher, 2011, 2013).

Moist Rayleigh-Bénard convection presents a statistical equilibrium state that differs significantly from that of the classic Rayleigh-Bénard convection. Pauluis and Schumacher (2011) shows that moist convection under conditionally unstable conditions self-aggregates in isolated turbulent cloudy patches separated by large quiescent dry regions, similar to those found in radiative-convective equilibrium simulations with more realistic models. In addition, the upward energy transport is barely higher than molecular diffusion, even when the Rayleigh number increases dramatically. The latter finding raises a fundamental question for our understanding of moist convection in the quasi-equilibrium regime: how can moist convection contribute significantly to the upward heat transport if it is directly affected by diffusion? In addition, vortices in MRBC may still share the similar the mechanism to enhance heat transport with Taylor vortices in standard rotating Rayleigh-Bénard convection. Cyclogenesis can be expected in the presence of rotation in the conditionally unstable layer settled by moist Rayleigh-Bénard convection.

The classic rotating Rayleigh-Bénard convection typically exhibits tall, thin, coherent convection columns that are aligned with the vertical direction (King et al., 2009;

R. J. Stevens et al., 2013). On the one hand, the presence of rotation restricts the area and horizontal scales of convective cells due to suppression by the Taylor-Proudman effect (R. J. Stevens et al., 2013; Zhong & Ahlers, 2010). On the other hand, R. J. Stevens et al. (2013) and Zhong and Ahlers (2010) show rotation can enhance the heat transport by Ekman pumping depending on the ratio of rotation time scale to the convective time scale, i.e., Rossby number. The initial development of a broad circulation proceeds according to the boundary layer that causes non-rotating self-aggregation (Wing et al., 2016), and the development of the Ekman layer may provide extra heat transport to the convection. The conditionally unstable layer satisfies some of the conditions of popular theoretical criteria for cyclogenesis. The maximum intensity of a vortex can be computed explicitly in the regime, and the estimation of maximum intensity provides us the way to understand the convection. The moist static energy provided at the lower boundary can be computed explicitly, so this can be a great indicator to estimate the strength of hurricane-like vortices relative to the hurricanes in the earth's atmosphere (Emanuel, 1986).

The purpose of this study is to understand the equilibrium state in rotating moist Rayleigh-Bénard convection, and to explore the dynamic similarity of the parameters to those of our earth's atmosphere. Section 2 introduces rotating moist Rayleigh-Bénard convection in the conditionally unstable layer and its numerical implementation. Section 3 demonstrates the relation between parameters in idealized simulation and the parameters in Earth's atmosphere, and the overview of MRBC in the presence of rotation following by the axisymmetric and isentropic analysis to the hurricane-like vortices. Section 4 presents the exploration of parameter space of rotating moist Rayleigh-Bénard convection.

2 Conditionally Unstable Moist Convection with Rotation

2.1 Model equations

We solve the three-dimensional Boussinesq-Navier-Stokes equations with the consideration of phase change of water vapor in a rotating frame constructed in Pauluis and Schumacher (2010). The equations are given by

$$\frac{d\mathbf{u}}{dt} = -\nabla p + \nu\nabla^2\mathbf{u} + B(D, M, z)e_z, \tag{1}$$

$$\nabla \cdot \mathbf{u} = 0, \tag{2}$$

$$\frac{dD}{dt} = \kappa\nabla^2 D, \tag{3}$$

$$\frac{dM}{dt} = \kappa\nabla^2 M. \tag{4}$$

Here, $\frac{d}{dt} = \frac{\partial}{\partial t} + u \cdot \nabla$ denotes the material derivative, u is the velocity field, p is the kinematic pressure, ν is kinematic viscosity, and κ is the scalar diffusivity. A dry buoyancy D and a moist buoyancy M are linear combinations of the total water content and the potential temperature on the unsaturated and saturated side of the phase boundary (Pauluis & Schumacher, 2010). The dry buoyancy field D is then proportional to the liquid water potential temperature and the moist buoyancy field M to the equivalent potential temperature. We apply the no-slip boundary condition for the flow at $z = 0$ and free-slip boundary condition for the flow at $z = H$. We assign Dirichlet conditions for dry and moist buoyancy with D_0, M_0 and D_H, M_H for two buoyancy fields, respectively, (Figure 1a). The buoyancy field B is defined as

$$B(x,t) = \max(M(x,t), D(x,t) - N_s^2 z), \tag{5}$$

with the fixed Brunt-Väisälä frequency N_s that is determined by the moist adiabatic lapse rate. When the layer is unsaturated, the buoyancy takes the dry buoyancy subtracted by Brunt-Väisälä frequency, and the buoyancy takes the moist buoyancy when the layer

is saturated. The non-linearity of Equation 5 captures the discontinuity in the derivative of buoyancy associated with the phase transition (Pauluis & Schumacher, 2010; B. Stevens, 2005). Given the stable stratified dry buoyancy and the unstable stratified moist buoyancy, Equation 5 can describe conditionally unstable moist convection. Condensed water is present whenever the moist buoyancy exceeds a saturation value and is given by

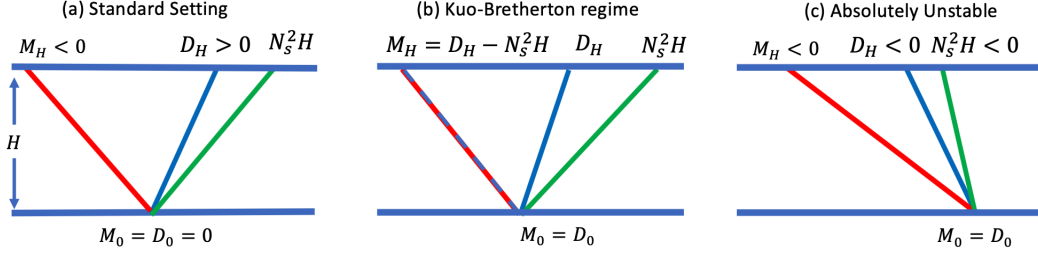$$CW(M, D, z) = \max(M - D + N_s^2 z, 0). \tag{6}$$

Figure 1. The vertical profile of moist buoyancy (red), dry buoyancy (green), and Brunt-Väisälä frequency (blue) in the transition to convective turbulence regime. (a) Configuration of a conditionally unstable boundary condition for moist Rayleigh-Bénard problem, i.e. $M_H < 0$ and $D_H > 0$. (b) A special case in conditionally unstable atmosphere, the Kuo–Bretherton (KB) equilibrium satisfies $M_H = D_H - N_s^2 H$ (dash blue). (c) Configuration of a linearly unstable equilibrium, where both D_H and N_s^2 are negative.

The moist Rayleigh-Bénard convection problem can be characterized by five nondimensional numbers and associated dimensionless equations. See Appendix A for the derivation. The convection is primarily characterized by two Rayleigh numbers, Ra_D and Ra_M, defined as

$$Ra_M = \frac{(M_0 - M_H)H^3}{\nu\kappa}, \quad \text{and} \quad Ra_D = \frac{(D_0 - D_H)H^3}{\nu\kappa}, \tag{7}$$

which quantify the buoyancy driving of the saturated and unsaturated buoyancy field M and D. Conditional instability occurs when the atmosphere is stably stratified for unsaturated parcels, but saturated parcels are convectively unstable, which translates to $M_H < 0$ and $D_H > 0$, as shown in Figure 1a. This implies the layer is conditionally unstable if $Ra_D < 0$ and $Ra_M > 0$. Since the diffusivities for moist and dry buoyancy are the same, there is only one Prandtl number, defined as

$$Pr = \frac{\nu}{\kappa}. \tag{8}$$

The Prandtl number is equal to 0.7 since we are interested in the convection in the atmosphere. Two more dimensionless numbers are tied to the saturation condition at the top and bottom boundary,

$$CW_0 = \frac{M_0 - D_0}{N_s^2 H} \quad \text{and} \quad CW_H = 1 + \frac{M_H - D_H}{N_s^2 H}. \tag{9}$$

While the MRBC problem is defined by these five non-dimensional numbers, most investigations have focused on constant Prandtl number ($Pr = 0.7$) and have assumed that the lower boundary is at saturation with $CW_0 = M_0 = D_0 = 0$ which can be interpreted as convection over an ocean. In such case, the parameter CW_H alone determine whether the diffusive equilibrium is saturated ($CW_H > 0$) or not ($CW_H < 0$). See Appendix A for the details. The case $CW_0 = CW_H = 0$ corresponds to a linear

diffusive profile which is at saturation but with no condensed water present, and is referred to as the Kuo-Bretherton case (Kuo, 1961; Bretherton, 1987, 1988). In this study, we set the environment to be in the Kuo-Bretherton equilibrium (Figure 1b). We define the convective velocity scale

$$w_s = \sqrt{H\left(M_0 - M_H\right)} \tag{10}$$

based on the maximum vertical velocity that can be achieved. See appendix A for the details.

Pauluis and Schumacher (2011) indicates that self-aggregated convection is characteristic of the conditionally unstable regime, and standard Rayleigh-Bénard convection is in the absolute unstable regime and rarely experiences self-aggregation. In the absolutely unstable regime, both dry and moist Rayleigh number are positive as demonstrated in Figure 1c. The absolutely unstable regime usually contains a homogeneous cloud layer with unstable dry buoyancy profile (Schumacher & Pauluis, 2010; Weidauer et al., 2010; Pauluis & Schumacher, 2010), or in the presence of radiation (Pauluis & Schumacher, 2013). Two types of convection show the different overturning structure. The overturning in the conditionally unstable layer presents an asymmetry of saturated updraft and unsaturated downdraft. In contrast, the overturning is symmetric in the absolutely unstable regime. This difference implies the development of convection in conditionally unstable layers rely on saturated updraft, whereas the convection in absolutely unstable layer does not require saturation.

2.2 Inclusion of rotation

The effect of rotation in the earth's atmosphere consists of centrifugal force and Coriolis force. In most geophysical applications, the centrifugal force is combined with gravity to form a geopotential and, in a Boussinesq model, its impact is included in the buoyancy term. For the Coriolis force, we consider the f-plane in our idealized simulation which yields the momentum equation:

$$\frac{d\mathbf{u}}{dt} + \nabla p + f e_z \times \mathbf{u} = \nu \nabla^2 \mathbf{u} + B(D, M, z) e_z, \tag{11}$$

where f is the Coriolis parameter and is fixed throughout the integration. Although the formulation of rotation is fundamental, our focus here is the evolution of the dynamical behavior of moist convection altered by the f-plane rotation.

In order to characterize the time scale of each physics component in MRBC in the presence of rotation, we use the standard way to define the time scale in Rayleigh-Bénard convection, and the comparison to real atmosphere will be discussed in section 3.1. We denote the diffusion time scale T_D, convection time scale T_C and rotation time scale T_R as

$$T_D = \frac{H^2}{(\nu\kappa)^{1/2}}, \quad T_C = \left(\frac{H}{M_0 - M_H}\right)^{1/2}, \quad \text{and} \quad T_R = \frac{1}{f}, \tag{12}$$

respectively. Note that the convective time scale corresponds to the convective velocity scale, w_s. In our simulation setting (Table 1), the convective time scale is about a few hundred seconds. The rotation time scale is a few hours and the diffusion time scale is a few days. The connection between the idealized simulation and the real atmosphere will be demonstrated in the results section.

We introduce two non-dimensional numbers to compare the time scale of convection, rotation, and viscosity: the convective Rossby number R_0 and the Ekman number E, defined as

$$R_0 = \frac{T_R}{T_C} = \sqrt{\frac{M_0 - M_H}{f^2 H}} \quad \text{and} \quad E = \frac{\nu}{f H^2}. \tag{13}$$

The convective Rossby number is the ratio of the inertial time scale to the convective time scale, which measures the importance of thermal forcing relative to the rotation.

Geostrophic theories suggest equilibrium when the Rossby number is small, whereas we can see the hurricane-like vortices have a moderate Rossby number, by measuring the convective time and the rate of rotation. The Ekman number measures the contribution of vertical flux induced by the rotating boundary layer. In our configuration, the rotating boundary layer appears only in the bottom boundary. Note that the convective Rossby number is selected to be the independent of other non-dimensional numbers in the later discussion, so the Ekman number is determined by the ratio of the convective Rossby number to the moist Rayleigh number.

2.3 Numerical Implementation

We use an adaptive mesh, variable-density incompressible Navier-Stokes solver (IAMR) to solve the equations governing moist Rayleigh-Bénard convection in the rotating frame; see Equations 1-4. IAMR (Almgren et al., 1998) was originally designed to solve the variable density incompressible Navier-Stokes equations using a second-order accurate projection method. It is based on the AMReX software framework (Zhang et al., 2021) that supports block-structured adaptive mesh refinement(AMR) for massively parallel applications. We have adapted IAMR to include dry and moist buoyancy terms. IAMR uses a fractional step approach: in the first step, an unsplit second-order approach is used to update velocity and scalars. In the second step, the provisional velocity field is updated with an approximate projection to (approximately) enforce the velocity divergence constraint and define the pressure at the new time. See Appendix B for details.

Our aim is to investigate how the moist convection balances the potential energy supplied at the boundaries. We initially define a constant density atmosphere with height $H = 1$ and horizontal extent L in both horizontal directions. We define the aspect ratio $A = L/H$. The viscosity is set to be 0.001, and the thermal diffusivity is set to be 0.0014, so that the Prantl number is 0.7 in our simulations.

The boundary condition for the velocity are free-slip at the top boundary and no-slip at the bottom boundary. The boundary conditions for moist and dry buoyancy at both top and bottom boundaries are Dirichlet. The moist Rayleigh number is controlled by the boundary conditions given at the top and bottom boundary, and the viscosity and diffusivity remain fixed. This environment is conditionally unstable, and in the Kuo-Bretherton equilibrium. In particular, $M_H = -3D_H$ and $D_H - M_H = N_s^2 H$. We apply a constant Coriolis parameter f in the simulation, and vary f from 0 to 0.1.

All of the simulations are initialized with a random perturbation on the moist and dry buoyancy specified at the bottom of the domain. This initial disturbance can induce a burst of convection, and this convection can sustain or dissipate depending on the moist Rayleigh number and the size of the domain. This setting is sufficient to investigate the transition in the presence of rotation and to study a hurricane-like vortex. Simulations are run up to a viscosity scale, which is around three hundreds convective time scale. The main experiments presented here are run in a domain of aspect ratio $A = 40$, resolved on a base mesh with 1280 cells in each horizontal direction and 32 cells in the vertical. The cases for parameter exploration run in a domain of aspect ratio $A = 20$ on a $640 \times 640 \times 32$ base grid.

3 Results

In this section, we present results from our moist Rayleigh-Bénard convection simulations with and without rotation. First, we compare the parameter ranges for atmospheric convection and moist Rayleigh-Bénard convection. Then, we explore the contribution of rotation to the convection from the snapshots, domain-averaged and time-averaged profiles of both non-rotating and rotating convection. We demonstrate the asymmetri-

cal profile hurricane-like vortices the isentropic analysis for both rotating and non-rotating convection.

3.1 Parameter ranges for atmospheric convection

The simulations of moist Rayleigh-Bénard convection presented here are highly idealized. Still, we would like to keep an explicit link between the non-dimensional parameters chosen here and the characteristics of tropical convection. We consider an equivalent MRBC case for deep convection by taking an atmospheric slab of 10km over an ocean as described above. As the vertical extent of deep convection is comparable to the scale height of density in the atmosphere, the use of the Boussinesq approximation is not accurate and a model with the anelastic approximation would be more suitable. With this caveat, we still provide here the magnitude of the dimensionless parameters corresponding to the theoretical vortex regime. The upper boundary condition as accounting for the exchange of air with an upper tropospheric cirrus layer in which energy is lost due to the emission of infrared radiation. The condensed water is removed through precipitation in the atmosphere, but we assume the condensed water is removed at the upper boundary in MRBC. We use the viscosity and diffusivity for dry air of $\nu = 1.5 \times 10^{-5} \ m^2 \ s^{-1}$ and $\kappa = 2.3 \times 10^{-5} \ m^2 \ s^{-1}$ respectively, resulting in a Prandtl number of $Pr = 0.7$.

We here follow the discussion in Pauluis and Schumacher (2013) to relate a given set of atmospheric conditions to the distribution of the dry and moist buoyancies in MRBC as well as the corresponding nondimensional parameters. For a given atmosphere between two layers, we determine the stability of the atmosphere by the Brunt-Väisälä frequency, N^2. The boundary conditions for the dry buoyancy can be obtained by specifying the linear profile of D_0 and D_H as

$$D_H - D_0 \approx N^2 H \quad \text{and} \quad Ra_D \approx -\frac{N^2 H^4}{\nu \kappa} \tag{14}$$

The Brunt-Väisälä frequency of the earth's atmosphere $N^2 = 0.01$ and the dry Raleigh number $Ra_D \approx -7.1 \times 10^{19}$. The moist buoyancy difference is rescaled by the convective velocity scale, w_s. This results in

$$M_0 - M_H = \frac{w_s^2}{H} \quad \text{and} \quad Ra_M \approx \frac{w_s^2 H^2}{2\nu \kappa}, \tag{15}$$

where the convective velocity scale is given at $100m/s$, so the moist Rayleigh number is $Ra_M = 4.3 \times 10^{20}$. Such a high Rayleigh number cannot be simulated with existing computing resources. The Rayleigh number of $Ra_M = 6.9 \times 10^6$ in most of our simulations of this study would correspond to viscosity and diffusivity of $\nu_{num} \approx 320 \ \mathrm{m^2 \, s^{-1}}$ and $\kappa_{num} \approx 457 \ \mathrm{m^2 \, s^{-1}}$. The corresponding time scale for viscosity T_D is 3 days. The typical value for turbulent viscosity in the planetary boundary layer varies from $1 \, \mathrm{m^2 \, s^{-1}}$ to $10 \, \mathrm{m^2 \, s^{-1}}$, and the Prandtl number for turbulent viscosity and turbulent diffusivity is approximately 0.74 (Stull, 1988). Our direct numerical simulation simulates a fairly more viscous atmosphere than the real atmosphere. The relative diffusion time scale and Ekman number correspond to moist Rayleigh numbers are shown in Table (1).

The convective Rossby number for the hurricanes in the earth's atmosphere is $O(10)$, and the time scale of convection is selected by convective velocity scale. Here, the time scale of rotation is selected at 15° N; i.e. $f = 5 \times 10^{-5}$. The convective time scale is then slightly shorter than the rotation time scale, so the convective Rossby number in the earth's atmosphere remains the same order in the idealized simulation.

3.2 Self aggregated convection in the presence of rotation

We demonstrate moist convection in the conditionally unstable layer, and Pauluis and Schumacher (2011) show that moist Rayleigh-Bénard convection in conditionally un-

Table 1. List of simulation parameters. For all runs the dry and moist Rayleigh numbers are related by $3Ra_D = -Ra_M$. The total integration time T equals the diffusive time scale T_D, the rotation time scale T_R is the inverse of Coriolis parameter, the convective time scale T_C is the large scale turnover time $T_C = \sqrt{H/(M_0 - M_H)}$, all of which defined in Equation (12).

Ra_M	$w_s(ms^{-1})$	T_C (s)	T_D (s)	ν_{num}	E_k (f = 0.05)
6.9×10^6	100	100	2.6×10^5	3.2×10^2	4.8×10^{-3}
1.7×10^6	100	100	1.3×10^5	6.4×10^2	9.6×10^{-3}
4.3×10^5	100	100	6.6×10^4	1.3×10^3	1.9×10^{-2}
1.1×10^5	100	100	3.3×10^4	2.5×10^3	3.8×10^{-2}
2.7×10^4	100	100	1.6×10^4	5.2×10^3	7.6×10^{-2}

stable layer shares the same characteristics as moist convection in the conditionally unstable layer. In Figure 2, we show two snapshots of the vertically integrated moist buoyancy, scaled by the maximum intensity $\frac{w_s^2}{2}$ generated by convective velocity scale, w_s. The left panel shows the results from a simulation without rotation, while the right panel shows the corresponding simulation for a nondimensional rotation $f = 0.05$, equivalent to the convective Rossby number, $R_0 = 6.2 \times 10^1$. The vertical integrated linear profile of moist buoyancy as shown in Figure 1b scaled by $\frac{w_s^2}{2}$ is -1, so the value greater than -1 corresponds to upward motion and the values less than -1 indicate subsiding.
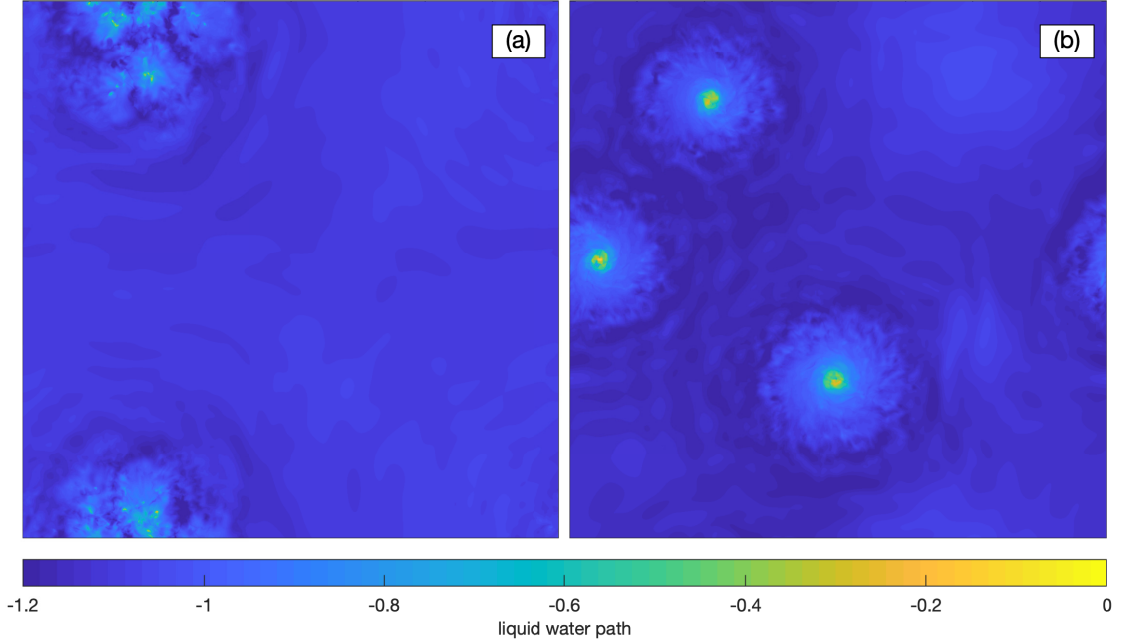

Figure 2. The instantaneous of vertical integrated moist buoyancy for the (a) $f = 0$ case and (b) $f = 0.05$ case in the $A = 40$ domain. The vertical integrated moist buoyancy is normalized by the linear profile.

In the absence of rotation, convection organizes into turbulent self-aggregated moist patches separated by quiescent dry regions, as shown in Figure 2a. The concentrated ascending region surrounded by slowly subsiding region implies that the convection is asymmetric with respect to the vertical direction. This self-aggregated system reaches a quasi-equilibrium status, since the convection is capable of sustaining itself by the potential energy given at the boundaries. Note that the equilibrium state is sensitive to the size of domain, where the convection in the small domain will develop an intermittent convection (Pauluis & Schumacher, 2011). The self-aggregation does not require any feedback from precipitation, surface flux or shortwave and longwave radiation that are usually required for self-aggregation in more physically realistic models (Wing et al., 2016) and is an intrinsic feature of the moist Rayleigh-Bénard convection under condition instability (i.e. for $Ra_M > 0$ and $Ra_D < 0$).

In the presence of rotation, the convection organizes into quasi-steady vortices, as shown in Figure 2b. Within each vortex, we can distinguish three separate regions: the rapidly ascending region in the center with high energy and moisture content, an outer moist region carrying by the flow outward away from the center, and a dry subsiding environment at the vortex boundary. In this simulation, the outer moist region has a diameter of about 100km. The diameter of the inner ascending region is about 20 to 30km, making the vortices substantially smaller then observed tropical storms. The ascending regions in the rotating case also exhibit very high values of moist buoyancy, close to the surface value M_0. This is indicative of very little mixing within this inner core, in contrast to the lower value found in the self-aggregated moist patches of the non-rotating case. At the same time, the subsidence region in the rotating case is significantly dryer than in the non-rotating case.

Figure 3 shows the 3-D snapshot of vertical velocity greater than 1% of the quantity scaled by convective velocity scale, w_s. We observe for both cases that most of the non-convecting region is near neutral and the vertical velocity of air parcels is less than $0.01\ w_s$. The downdrafts in the subsidence region of self-aggregated convection and hurricane-like vortices are also less than $0.01\ w_s$. In the non-rotating case, we observe the updraft and downdraft randomly distributed in self-aggregated cloud clusters. This distribution can be referred to as vertical integrated moist buoyancy which contains high moist buoyancy and low moist buoyancy in the patch of cloud clusters in Figure 2. In the rotating case, we observe a strong updraft in the center of a vortex. In the outer region, the instantaneous updraft and downdraft show a ring structure, despite the rather uniform distribution of the integrated moist buoyancy.

The inclusion of rotation has a striking impact on the strength of the atmospheric flow. Figure 4a shows the time series of averaged kinetic energy. In both rotating and non-rotating cases, an initial burst of convection is followed by a slow decay, before convection intensifies again and the atmosphere settles into a statistical equilibrium. The average kinetic energy in the rotating case is, however, about two orders of magnitude larger than in the non-rotating case.

Figures 4b and 4c show the horizontal and vertical components of the kinetic energy, separating the contributions from the saturated (dashed line) and unsaturated (solid line) regions. The difference in kinetic energy arises primarily from the horizontal component of the flow in the unsaturated region. Figure 4e shows the saturated area take less than 20% among all levels and most regions are in the upper part of domain. The unsaturated region shows a weaker contribution to the vertical component of kinetic energy, but a stronger contribution to the horizontal component. In the presence of rotation, both ascending updrafts and descending downdrafts can generate rotational motion by stretching of the planetary vorticity. The descending region corresponding to the unsaturated parcel generates more rotational motion leading to the accumulation of horizontal kinetic energy over time.
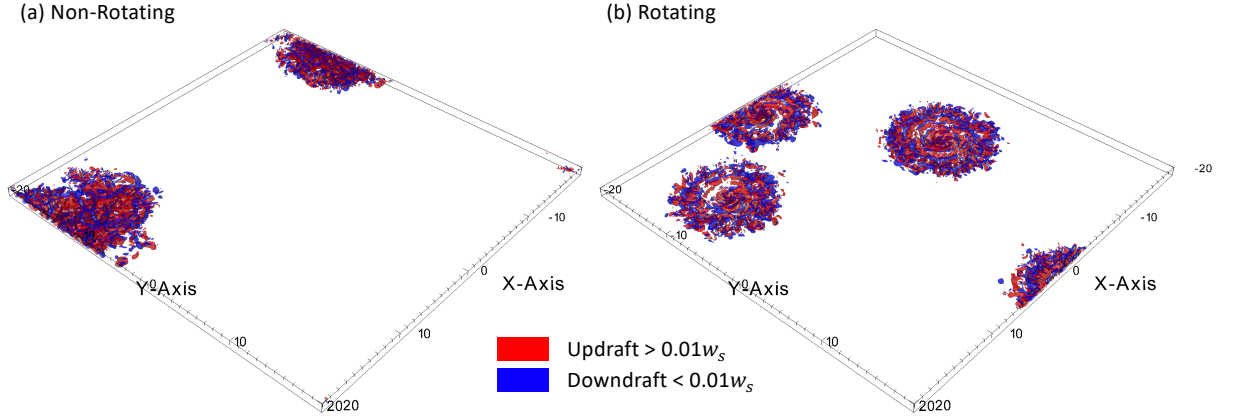
(a) Non-Rotating

(b) Rotating

Updraft > $0.01w_s$

Downdraft < $0.01w_s$

Figure 3. Instantaneous updraft and downdraft on the convective velocity scale, w_s, in the absence of rotation (a) and in the presence of rotation(b). The updraft and downdraft are plotted when its value is greater than 1% of w_s.

The vertical buoyancy fluxes are shown in Figure 4d. The upward buoyancy flux is dominated by the contribution from the saturated regions, i.e. the ascent of warm, moist air from the surface, while the unsaturated regions exhibit little density variation and thus do not contribute substantially to the generation of kinetic energy. Both non-rotating and rotating cases show a similar vertical buoyancy flux, albeit the flux is is slightly stronger (20%) in the later case. In particular, the difference in buoyancy flux is small compared to the difference in kinetic energy, so one cannot explain the intensification of the circulation in the rotating case by the extra vertical buoyancy flux. Rather, it appears that, in the presence of rotation, a substantial amount of kinetic energy ends up in horizontal rotational motion, which is less affected by frictional dissipation, therefore allowing a build-up of kinetic energy over time.

3.3 Vortex structure in rotating Moist Rayleigh-Bénard convection

The vortices that emerge in rotating Rayleigh-Bénard convection exhibit many of the characteristics of tropical cyclones in the Earth's atmosphere as well as some important differences. We define the center of a vortex as the average over all coordinates with
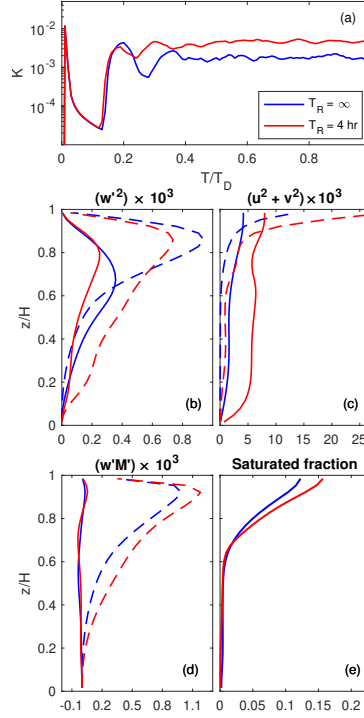
Figure 4. (a) The time series of total kinetic energy for the non-rotating and the non-rotating case. (b) The time-averaged vertical contribution of kinetic energy in the unsaturated region (solid line) and in the saturated region (dash line). (c) The time-averaged horizontal contribution of kinetic energy. (d) The time-averaged vertical buoyancy flux contribution. (e) The time-averaged kinetic energy flux contribution. The time-averaged profile averaged over the day 4 to day 8.

moist buoyancy larger than the threshold at 8km height, where the threshold is defined as the parcel greater than 70% of all parcels, i.e. $0.3(M_0 - M_H)$. When multiple vortices are present, they are first separated using a k-mean clustering algorithm. Figure 5 shows the azimuthal average over the last four days of total integrated time over all vortices.

Figure 5a shows the vertical velocity (shading) and cloud water content (white contour). The cyclone exhibits strong ascending motion at its center; the ascending motion is tilted, narrower at lower levels and broader in the upper half of the domain. We also observe subsidence surrounding by the updrafts at the center of vortex, similar to that found in the eye of a tropical storm. Away from the storm center, we observe a broad region of weak ascent in the upper half of the layer, and weak subsidence in the lower half. In Figure 5b, the radial average of vertical velocity shows a uniform updraft in the center of the vortex, with surrounding updrafts and downdrafts as shown in Figure 3. High liquid water content is found in the ascending region in the storm center and extends radially near the upper boundary. The vortex structure is highly reminiscent of many aspects of the Earth's tropical cyclones, including the tilted eyewall structure, subsidence in the storm center and extensive upper level stratiform clouds.

The horizontal extent of the vortex, however, is smaller than tropical storms, as the eyewall has a radius about 10 km - which would correspond to a storm diameter of about 20km, and the upper level cloud deck extends to a distance of 40 km from the storm
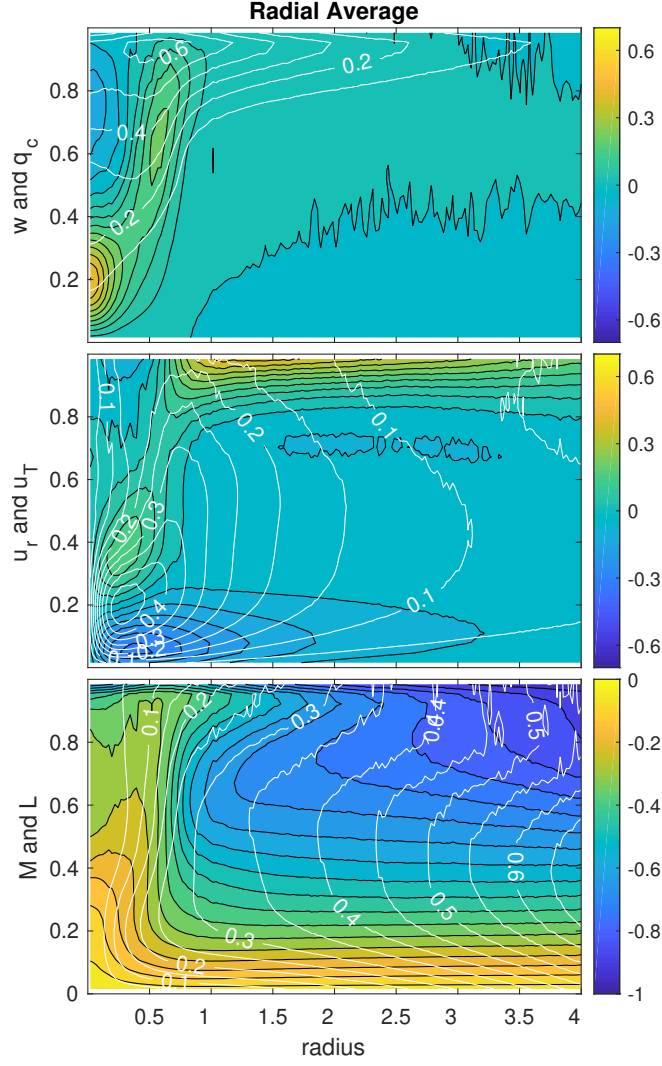
Figure 5. The axisymmetric structure of a vortex in Figure 2b. (a) The top panel shows the vertical velocity (shading) and the liquid water content (contour). (b) The middle panel shows the radial velocity (shading) and the tangential velocity (contour). (c) The bottom panel shows the moist buoyancy (shading) and angular momentum (contour). The center is located by averaging location of the first 1000 smallest moist buoyancy at the 25-th level. The vortices are separated by the clustering K-mean algorithm by MATLAB.

center. The velocity in Figure 5 is scaled by the convective velocity scale, so the maximum vertical velocity is 60% of w_s, which corresponds to 25 m/s.

In Figure 5b, we show the radial and tangential winds. The circulation exhibits a strong inflow at the bottom and outflow at the top boundary. We also observe a secondary inflow in the upper portion of the layer, but it is much weaker then the inflow at the bottom boundary. The maximum tangential wind appears near the lower boundary, and the magnitude is also 60% of convective velocity scale and (25 m/s) at about 3 km height and 10 km from the center of the vortex.

Figure 5c shows the moist buoyancy and angular momentum. The angular momentum L is defined as

$$L = r u_T + \frac{1}{2} f r^2, \qquad (16)$$

where r is the radius and u_T is the tangential velocity. The vortex brings high energy air parcels to the top of boundary. The moist buoyancy in our idealized framework acts in a very similar fashion to the moist entropy in a full physics model. Near the center of the storm, the angular momentum and iso-M surfaces of moist buoyancy are tilted and closely match, consistent with the hypothesis of slantwise convection in the eyewall of tropical storms Emanuel (1986). Nevertheless, we also observe that mixing remains significant as the highest moist buoyancy parcels do not really reach the upper boundary.

3.4 Isentropic analysis for Moist Rayleigh-Bénard convection

As noted before, rotating MRBC exhibits a substantial increase in the upward buoyancy flux. To better assess the enhancement of the buoyancy flux, we apply the isentropic analysis method by sorting the ascending air parcels according to their thermodynamic properties. This method takes advantage of fact that updrafts have higher moist buoyancy (similar to the sorting of the air parcels in terms of their moist entropy or equivalent potential temperature) than the subsiding air in moist Rayleigh-Bénard convection (Pauluis & Mrowiec, 2013; Mrowiec et al., 2016). To do so, the properties of the flow at each level z are conditionally averaged on the moist buoyancy M, which shares the property with equivalent potential temperature in the moist thermodynamics. Therefore, the horizontal coordinates (x, y) are replaced by one thermodynamic coordinate M while the dependence on height is retained. Here, we define an isentropic integral of any function f as the integral at a given vertical level on a given isentropic surface:

$$\langle f \rangle (z, M_e, t) = \int \int_{\Gamma} f(x, y, z, t) \delta \left\{ M_e - M(x, y, z, t) \right\} dx dy, \qquad (17)$$

where $\delta \left\{ \cdot \right\}$ is the Dirac delta function. The horizontal integral is taken over the domain Γ. The reference moist buoyancy M_e is treated as a constant parameter.

The probability density function, P, for a parcel with moist buoyancy at level z can be estimated as

$$P(z, M_e, t) = \int \int_{\Gamma} \delta \left\{ M_e - M(x, y, z, t) \right\} dx dy. \qquad (18)$$

The logarithm of the probability density function is shown in Figures 6a and 6b. The diagonal line shows the saturation condition, so the parcels above the line are saturated and the parcels below are unsaturated. The initial condition is given at the diagonal line, and the convection adjusts the vertical profile by transporting more buoyant parcels from the bottom of domain. The bulk of the PDF is concentrated around a curve to the left of the diagonal, corresponding to the equilibrium environment adjusted by the convective system. The majority of parcels at each level are unsaturated and these parcels form the subsidence that increases the stability in the lower atmosphere.

We observe the asymmetry of the distribution between the updrafts and downdrafts. The rising parcels observed are associated with very low probability compared to the sinking parcels with very high probability. The updrafts appear in the saturated parcel that is higher than the linear profile, and the downdrafts appear in unsaturated parcels, which is lower than the linear profile. The parcels with high moist buoyancy reach all the way from the surface to the top, while parcels with low moist buoyancy are mostly confined to the upper part of the domain. The distribution of downdrafts is two orders of magnitude higher than the distribution of updrafts.

In the presence of rotation, we observe a secondary maximum of parcels with high moist buoyancy. These parcels are separated from the mean environment, and indicate
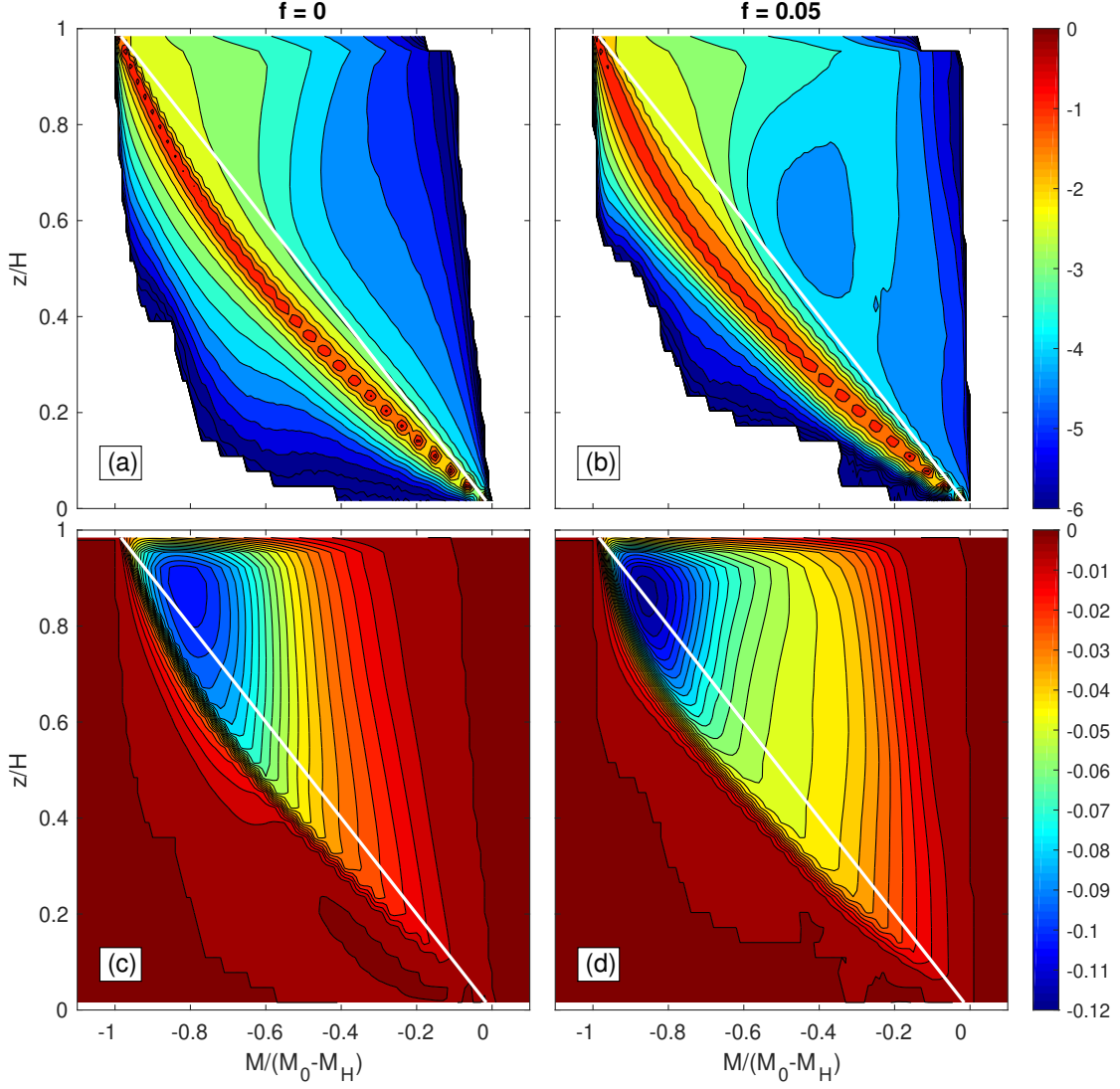
Figure 6. The time-averaged isentropic probability distribution function (upper panels) and isentropic streamfunction for cases in $A = 40$ (lower panels) in the absence of rotation (left panels) and in the presence of rotation (right panels). The air parcels below the white line are unsaturated, and above the white line are saturated.

the presence of a warm core in the vortex and moist vortex core. The probability for high buoyancy parcels is much higher with rotation compared to no rotation. We speculate the formation of the eyewall prevents mixing of high buoyancy updrafts with the low buoyancy downdrafts, and provides better heat transport through the core.

The mass flux is approximated by substituting $f = \rho w$ and averaging ρw over the finite size M bins ($\Delta M = 1\%$ of $M_0 - M_H$), so $\delta \{M_e - M\} \sim 1/\Delta M$. This process is repeated at each time step and each level. The mass flux can be integrated to obtain the isentropic streamfunction Ψ_M

$$\Psi_M(M, z, t) = \int_{-\infty}^{M} \langle \rho w \rangle (z, M', t) \, dM', \tag{19}$$

which corresponds to the net upward mass flux of all parcels with a moist buoyancy less than or equal to M.

Figures 6c and 6d show the isentropic streamfunction for the non-rotating and rotating cases averaged for the last 2 days of the simulation. The white line indicates the linear diffusive profile of moist buoyancy. The streamfunction corresponds to the mean trajectories in $M - z$ coordinates, and its negative value here corresponds to counterclockwise rotation, i.e. air rises at high values of M and subsides at lower values. In this case, it also separates between saturated (to the right) and unsaturated parcels (to the left), indicating that most of the ascending parcels are saturated, while most of the descending parcels are unsaturated.

We observe a more intense overturning streamfunction in the rotating cases than in the non-rotating case. The rotating case exhibits a stronger overturning than the non-rotating case, with a 20% increase in the magnitude of the streamfunction. In the rotating case, buoyant parcels can rise from the lower layer to the top of boundary without experiencing much dilution, as evidenced by the fact that the rightmost streamlines of the streamfunction in Figure 6d are almost vertical. In contrast, in the non-rotating case, these streamlines are tilted to the left, indicating that rising air parcels from the lower boundary tend to lose buoyancy as they rise as a result of their mixing with surrounding dry air. In the descending region, the rotating case takes a longer distance to return the average, so the formation of vortices prevents the mixing in both ascending and descending region. In the non-rotating case, we observe that some parcels take a longer distance than the average parcels to return to the surface. These parcels could be the rapid subsiding parcels near the center of cloud cluster in Figure 2a.

The presence of rotation improves the heat transport in moist Rayleigh-Bénard convection, but the heat transport remain bounded as proved in Pauluis and Schumacher (2011). In Figure 4, we observe the difference in the total kinetic energy; the energy transport shows a similar vertical pattern. The formation of vortices helps the convection store the kinetic energy in the horizontal component, and the horizontal kinetic energy is harder to dissipate. Thus, the maximum of the isentropic streamfunction in the rotating case is achieved. However, the heat transport in both cases remains bounded by the Nusselt number argument (Pauluis & Schumacher, 2011). The non-dimensional Nusselt number, measuring the heat transport, is approximated to $Ra^{\frac{1}{2}}$ or $Ra^{\frac{1}{3}}$ depending on the Rayleigh number, but the Nusselt number of conditionally unstable moist Rayleigh-Bénard convection is bounded by $\frac{Ra_D}{Ra_M}$ (Pauluis & Schumacher, 2011). In conditionally unstable convection, stabilization occurs when the dry stability becomes sufficiently strong to prevent even the ascent of saturated parcels for both rotating and non-rotating case (Pauluis & Schumacher, 2011).

The separation of updraft and downdraft induces an emergence of adiabatic ascent in the rotating case as found in the isentropic analysis of hurricanes (Mrowiec et al., 2016). The rotating case shows more efficient energy transport, as shown in Figure 4a. In Figure 4d, the contribution to the vertical buoyancy flux shows 20% more than the non-rotating case in the saturated region. In Figure 2, we observe the separation of updraft in the center of vortices and the subsidence located at the edges. This separation prevents the high buoyancy parcel from mixing with the low buoyancy parcel, as shown in Figure 6. Therefore, the additional vertical buoyancy flux and the separation of updraft and downdraft result in efficient vertical energy transport in the presence of rotation.

4 Sensitivity of rotating MRBC to rotation rate and Rayleigh numbers

The inclusion of rotation in conditionally unstable convection can lead to the emergence of intense vortices that share many similarities with tropical cyclones. We now in-

vestigate the parameter space of moist Rayleigh-Bénard convection to identify the conditions necessary for the presence of hurricane-like vortices. First, we study the competitive influence of rotation, convection, and diffusion, by simultaneously varying the Rayleigh number and convective Rossby number. Second, we investigate the role of the ratio of dry to moist Rayleigh number in the conditionally unstable Kuo-Bretherton regime.

4.1 The exploration of moist Rayleigh number and rotation rate

In this section, we vary the moist Rayleigh number and rotation rate to assess the effect on the presence of hurricane-like vortices. The ratio of the dry to the moist Rayleigh number is fixed as $Ra_D = -3Ra_M$, while we maintain saturation both at the upper and lower boundaries. The Prandtl number is 0.7 in all experiments, and the aspect ratio of the domain is $A = 20$. We investigate the parameter space by performing 25 simulations covering 5 different values of the Rayleigh number and 5 different rotation rates. The Rayleigh number ranges from 2.7×10^4 to 6.9×10^6, covering the transition from weakly non-linear convection to turbulent flow.

The parameter range in our simulation can be recast in dimensional units, as shown in Table 1. To obtain the dimensional units, we assume here that the convective velocity scale is taken to be $w_s = 100$ m/s in all simulations. This corresponds to a dimensional time scale of 100 seconds, assuming a layer depth of 10000 m. The Rayleigh number ranging from 2.7×10^4 to 6.9×10^6 corresponds to reducing the viscosity ν_{num} from 5200 to $320 m^2/s$. The rotation rate here varies from 0 (no rotation) to 0.1 non-dimensional units; the latter value corresponds to a dimensional Coriolis parameter of $10^{-4} s^{-1}$. The convective Rossby number depends on the combination of the Rayleigh number and rotation rate. In the experiment discussed here, it ranges from infinity, in the absence of rotation, to one for the lowest Rayleigh number and highest rotation rate. Simulations in which hurricane-like vortices are found exhibit a convective Rossby number of about 100.

Figure 7 plots snapshots of the vertical integrated moist buoyancy for different Rayleigh number (horizontal axis) and Coriolis parameter (vertical axis). These simulations exhibit a wide range of behavior. Here, we categorize into four different regimes: intermittent convection (I), self-aggregation (S), diffusive vortices (D), and tropical cyclones-like vortices (TC); the regime is indicated by the corresponding symbol ('I','S','D' and 'TC') on the upper left corner of each figure. These regimes are empirical, and are discussed in greater detail below. Several simulations exhibit characteristics of two or more regimes and are left unmarked.

The self-aggregation (S) and intermittent (I) regimes occur at low rotation rate, and are also found in the simulations of conditionally unstable convection discussed in Pauluis and Schumacher (2011). In the self-aggregated regime (S), convection aggregates into a large turbulent saturated patch separated by large unsaturated and quiescent areas. The fraction of the domain covered by self-aggregated patches becomes smaller as the Rayleigh number increases. For small domain or large enough Rayleigh number, there is insufficient area for the self-aggregated patch to be sustained in a quasi-steady state. In such cases, an intermittent regime (I) emerges, characterized by a sudden burst of intense localized convective activity separated by much longer quiet periods. These periods act to recharge the atmosphere, in terms of both its water content and its available potential energy, which is then rapidly discharged during short but intense convective outbursts. The non-rotating convection reaches self-aggregated convection in the larger domain, and intermittent convection in the smaller domain (Muller & Held, 2012; Wing et al., 2017). Non-rotating moist Rayleigh-Bénard convection shows the dependency on the moist Rayleigh number in a fixed domain aspect ratio.

In the presence of rotation, sustained convective motions can generate strong localized vortices. For traditional Rayleigh-Bénard convection, the inclusion of rotation
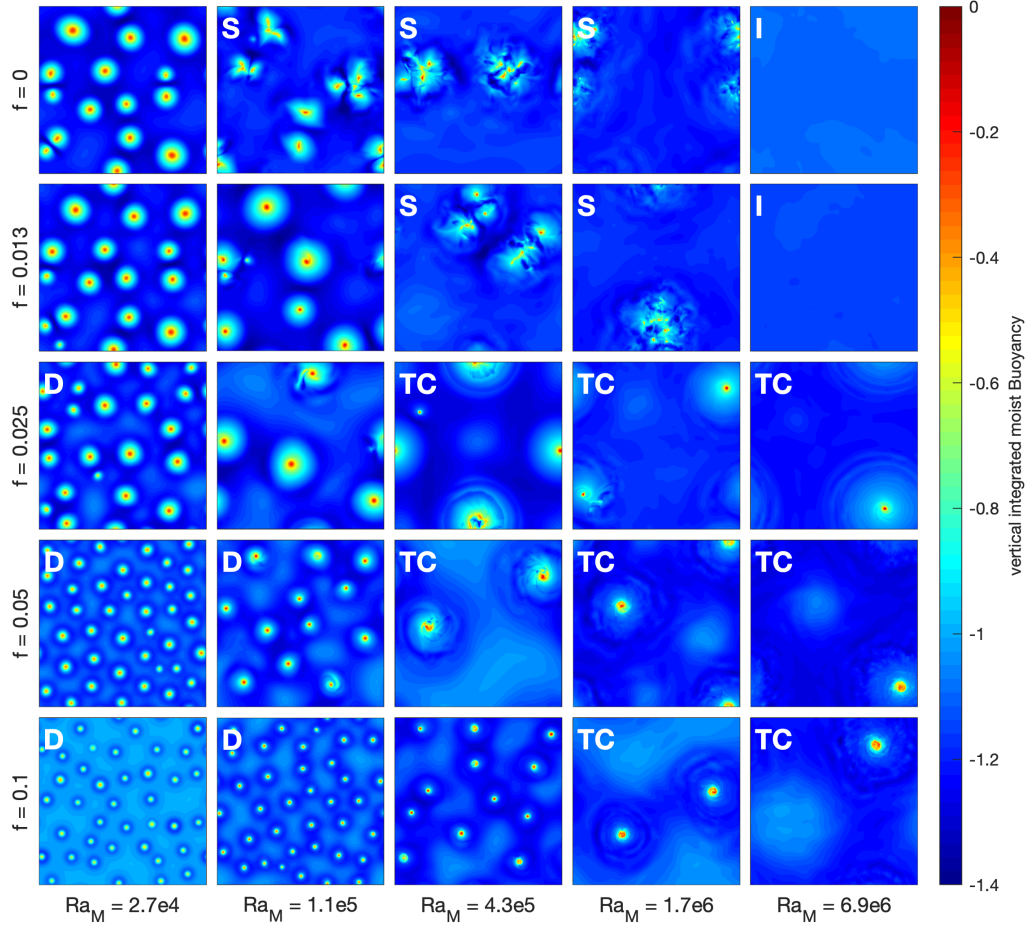
Figure 7. The instantaneous vertical integrated moist buoyancy for different moist Rayleigh number and Coriolis parameter in the KB regime. Note that this snapshot is taken at the last step of time integration, so the non-rotating case with $Ra_M = 6.9 \times 10^6$ is in the discharge phase. The equilibrium regimes are labeled, and please see texts for the explanation.

leads to the development of balanced vortices. These vortices are associated with secondary circulation characterized by an Ekman flow at both the upper and lower boundary, which can enhance the overall energy transport, at least at intermediate values of the convective Rossby number (R. J. A. M. Stevens et al., 2009; Zhong & Ahlers, 2010). At high rotation rates however, vortices becomes smaller and are more heavily affected by diffusion, resulting in a weakening of convection. In Figure 7, we distinguish between two regimes: the diffusive vortices (D), and the tropical-cycle line vortices (TC). The diffusive vortices in Figure 7 exhibit many similarities to the classic rotating Rayleigh-Bénard convection, including their spatial confinement, and the emergence of a balanced flow and of a secondary circulation. The rotation stabilizes the intermittent convection, so all the vortices regimes are in the quasi-equilibrium status.

587 The category TC occurs for intermediate values of the convective Rossby number
588 and large moist Rayleigh number. The primary difference with the diffusive vortices regime
589 (D) is that the area occupied by convection is substantially reduced in the TC regime.
590 As discussed in Pauluis and Schumacher (2011), for non-rotating convection under con-
591 ditional instability, an increase in the moist Rayleigh number results in a decrease in the
592 fractional area occupied by convective cells. We observe here a similar behavior for the
593 rotating case in that an increase in the Rayleigh number at constant rotation rate leads
594 to an increase in the spatial separation between vortices. Alternatively, if one holds the
595 Rayleigh number constant while gradually increasing the rotation rate, self-aggregated
596 convective patches develop some rotation and turn into coherent vortices. This strongly
597 suggests that rotating moist convection in a conditionally unstable environment should
598 spontaneously generate hurricane-like vortices.

599 The TC regime is characterized by strong coherent vortices supported by a meso-
600 scale secondary circulation. Figure 8 shows the time-averaged Eulerian streamfunction
601 vs. the radial coordinate for the four cases with two highest Rayleigh numbers and ro-
602 tation rates corresponding to the four panels at the bottom right of Figure 7. The Eu-
603 lerian stream function is defined as

$$\Psi_E(z, r) = \frac{2\pi r}{T_2 - T_1} \int_{T_1}^{T_2} \int_0^z \left[\rho v(r, z, t')\right] dz' \, dt', \tag{20}$$

604 where v is the radial wind and T_1 and T_2 is the selected time. The velocity here is scaled
605 by the convective velocity scale. All four cases exhibit a strong vortex at the center (white
606 lines) as well as a secondary circulation that extends well beyond the region of strong
607 vorticity. The outflow is confined to a shallow layer, while the inflow is split between a
608 low level inflow near the surface and an upper level component. Similar upper level in-
609 flows have been noted in realistic simulations of tropical cyclones as well (Mrowiec et al.,
610 2016; Pauluis & Zhang, 2017). The depth of the Ekman layer at the lower boundary is
611 directly affected by viscosity and is expected to be proportional to $Ra_M^{-1/4}$, which is con-
612 sistent with increased confinement of the inflow and outflow at the upper and lower bound-
613 ary seen in Figure 8.

614 The horizontal extent is also strongly affected by the combination of the rotation
615 rate and Rayleigh number. For a fixed moist Rayleigh number, the horizontal scale de-
616 creases as rotation rate increases, which is consistent with the notion that the size of the
617 vortex varies as the Rossby deformation radius and is thus proportional to f^{-1}. Figure
618 8 also indicates that the storm size increases with the Rayleigh number. Assuming that
619 in the subsidence region, the diabatic warming is balanced by vertical diffusion

$$w\frac{\partial D}{\partial z} = \kappa \frac{\partial^2 D}{\partial z^2},$$

620 indicates that the subsidence velocity w scales as κ or $Ra_M^{1/2}$ for a constant Prandtl num-
621 ber. Consequently, if the magnitude of the mass transport by the secondary circulation
622 is unchanged, then the expected radius of the storm should scale as $w^{-1/2} \approx Ra_M^{-1/4}$.
623 We only note here a qualitative agreement between this scaling and the result shown in
624 Figure 8, and a more complete investigation here is necessary to fully assess how the sec-
625 ondary circulation responds to change in rotation rate and Rayleigh number.

4.2 The isentropic streamfunction

627 To better assess the change in convective overturning in our simulations, we ap-
628 ply the isentropic analysis method by partitioning the properties of the flow in terms of
629 the moist buoyancy. In Figure 9, we show the probability distribution function (see Equa-
630 tion 18). The characteristics of moist convection are verified within a broader range of
631 parameters. The bulk of the PDF of all the categories is concentrated to the left of the
632 diagonal line. This corresponds to the equilibrium of the moist convection system, where
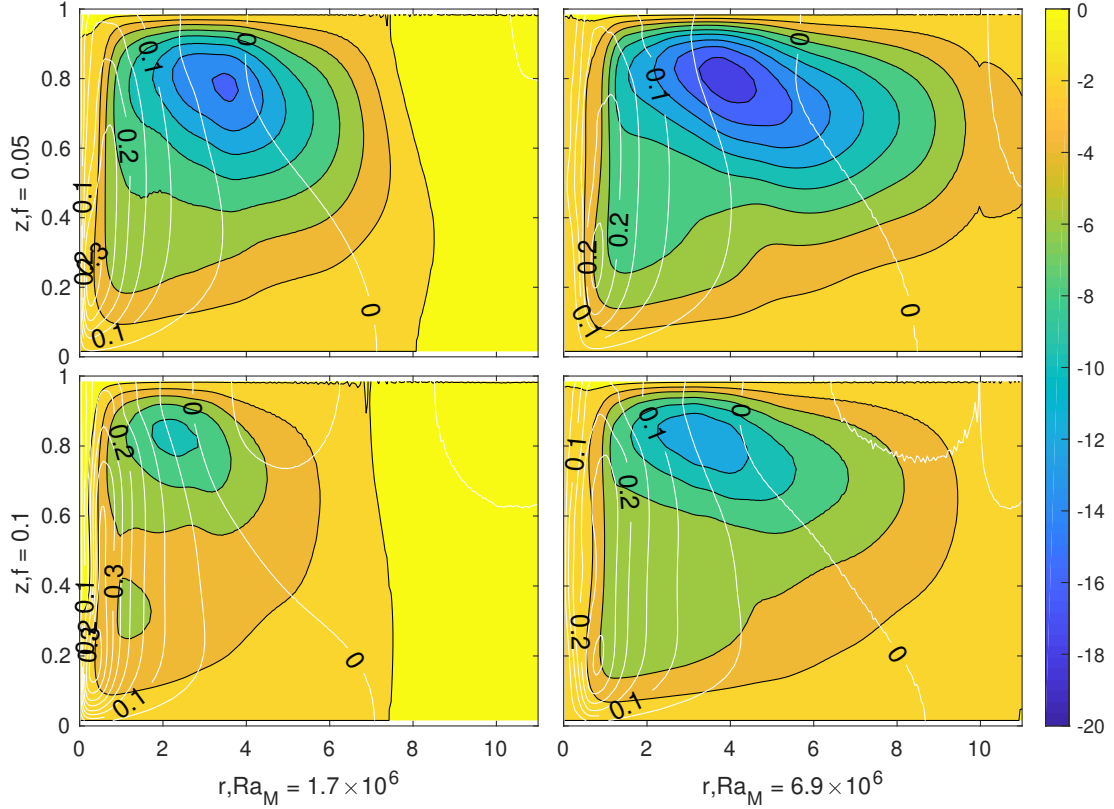
Figure 8. The time-averaged Eulerian stream function (shading) and tangential velocity(contours) for cases in the tropical-cyclone regime(TC).

the majority of parcels are unsaturated. Figure 9 also shows the parcels with high buoyancy reach all the way from the surface to the top, whereas the low buoyancy parcels are confined to the upper part of domain. These two features have already been discussed in Section 3 and highlight that the asymmetry between updraft and downdrafts is a fundamental difference – that persists through a broad range of parameters – between moist Rayleigh-Bénard convection in the conditionally unstable layers and standard Rayleigh-Bénard convection.

While all 25 simulations presented here exhibit many similar features, they also show some important differences. In the self-aggregated regime, the PDF indicates that parcels with low moist buoyancy - characteristic of the upper boundary - can be found at low levels. This shows that, in self-aggregated convection, convective downdrafts stretch the entire depth of the layer. This is noteworthy, as a parcel with the moist and dry buoyancies characteristics of the upper boundary would be positively buoyant through the entire layer. Hence, bringing such a parcel from the bottom to the top requires strong mechanical mixing to compensate for the parcel's buoyancy. In contrast, in the tropical cyclone (TC) and dissipative (D) regimes, parcels with low moist buoyancy are restricted to the middle layers, indicating that strong convective downdrafts are prevented through a combination of rotation and diffusion.

A second noteworthy difference lies in the emergence of a secondary maximum in the PDF at high values of the moist buoyancy in the TC regime. The minimum of probability appears in the middle layer as found in Figure 6. As strong vortices develop, gradient wind balance makes it possible to develop a large buoyancy gradient across the do-

main, this allowing the presence of a warm, moist vortex core, surrounded by a colder
and dryer environment. At the same time, the strong rotational winds act as a mixing
barrier to prevent direct mixing between the two air masses. In contrast, other categories
show a distribution with a single maximum at each level corresponding to the charac-
teristics of the environment. In the absence of rotation (regimes I and S), it is not pos-
sible to sustain a large buoyancy gradient, and warm, moist air parcels all rise rapidly
to the upper boundary. In the diffusive vortex regime, diffusion acts to rapidly destroy
the horizontal density variation. Thus, in our findings, the TC regime emerges from a
combination of strong enough rotation and weak diffusion that allows for the formation
of warm core vortices, which can be readily identified in the isentropic analysis.

Figure 9. The time-averaged isentropic probability density function for cases in $A = 20$.

While the PDF characterizes the area covered by air parcels with different ther-
modynamic properties, the isentropic streamfunction offers a straightforward insight into

the atmospheric overturning. The isentropic streamfunction is shown in Figure 10 and indicates a dramatic weakening of the overturning as the Rayleigh number increases. While this may seems counter-intuitive given the fact that in the classic Rayleigh-Bénard problem, convection intensifies as the Rayleigh number increases, this behavior is fully consistent with the fact that, for conditionally unstable conditions, convection becomes increasingly intermittent as the Rayleigh number increases (Pauluis & Schumacher, 2011). Thus, the weakening of the overturning shown in Figure 10 does not arise from the fact that convection is becoming weaker, but rather it is due to the fact that the area of active convection only occupies a small fraction of the domain as the Rayleigh number increases, as evidenced by Figure 7.

Before explaining in greater detail the weakening of the overturning with increased Rayleigh number, it must be noted that the streamfunction (Equation 19) is computed here using non-dimensional equations in which the vertical velocity is rescaled by the convective velocity scale w_s. The upward transport of moist buoyancy transport can be defined as $\overline{wM}$, where the overline denotes a horizontal average. It can also be estimated from the horizontal integral of the streamfunction as

$$\overline{wM} = -\int \Psi(M, z)\, dM. \tag{21}$$

The streamfunction in Figure 10 exhibits a similar structure, with a broad region of negative value between M_0 and M_H. This yields a scaling for the heat flux as

$$\overline{wM} = (M_0 - M_H)\Delta \widetilde{\Psi}_M, \tag{22}$$

where $\Delta \widetilde{\Psi}_M$ is (minus) the amplitude of the streamfunction. In particular, the amplitude of the streamfunction should scale as the upward moist buoyancy flux.

Under conditional instability conditions, Pauluis and Schumacher (2011) argue that the upward energy transport remains limited by diffusion. They argue that the vertical gradient of dry buoyancy at the lower boundary cannot exceed N_s^2, the Brunt-Väisälä frequency associated with saturated ascent, which is equivalent to requiring that there is no convective inhibition at the lower boundary. However, as the upward energy flux is equal to the diffusive energy flux at the lower boundary, this yields an upper bound on the upward energy transport,

$$\overline{wM} = \kappa \left.\frac{\partial M}{\partial z}\right|_{z=0} \leq \kappa \frac{N_s^2 H}{D_H - D_0}(M_0 - M_H). \tag{23}$$

If we combine this with the scaling for the streamfunction in Equation 22, we obtain an upper bound for the overturning as

$$\Delta \widetilde{\Psi}_M \leq \frac{N_s^2 H}{D_H}\kappa. \tag{24}$$

In the experiments discussed here, the ratio $\frac{N_s^2 H}{D_H}$ has been held constant and is equal to 4. The amplitude of the streamfunction $\Delta \widetilde{\Psi}_M$ is thus proportional to the diffusivity κ. In the non-dimensionalized equations, diffusivity scales as the square root of the Rayleigh number, which explains the weakening of the isentropic streamfunction as the Rayleigh number increases.

Increasing the Rayleigh number in a conditionally unstable moist Rayleigh-Bénard convection problem leads to a decrease in the atmospheric overturning as convection becomes increasingly intermittent. From a physical point of view, under conditionally unstable conditions, stabilization can be done by reducing the overall saturation of the layer and increasing the (dry) static stability at the lower boundary, and can be achieved by redistributing only a small fraction of the layer. This is in contrast to the classic Rayleigh-Bérnard convection in which stabilization requires mixing of the entire layer.
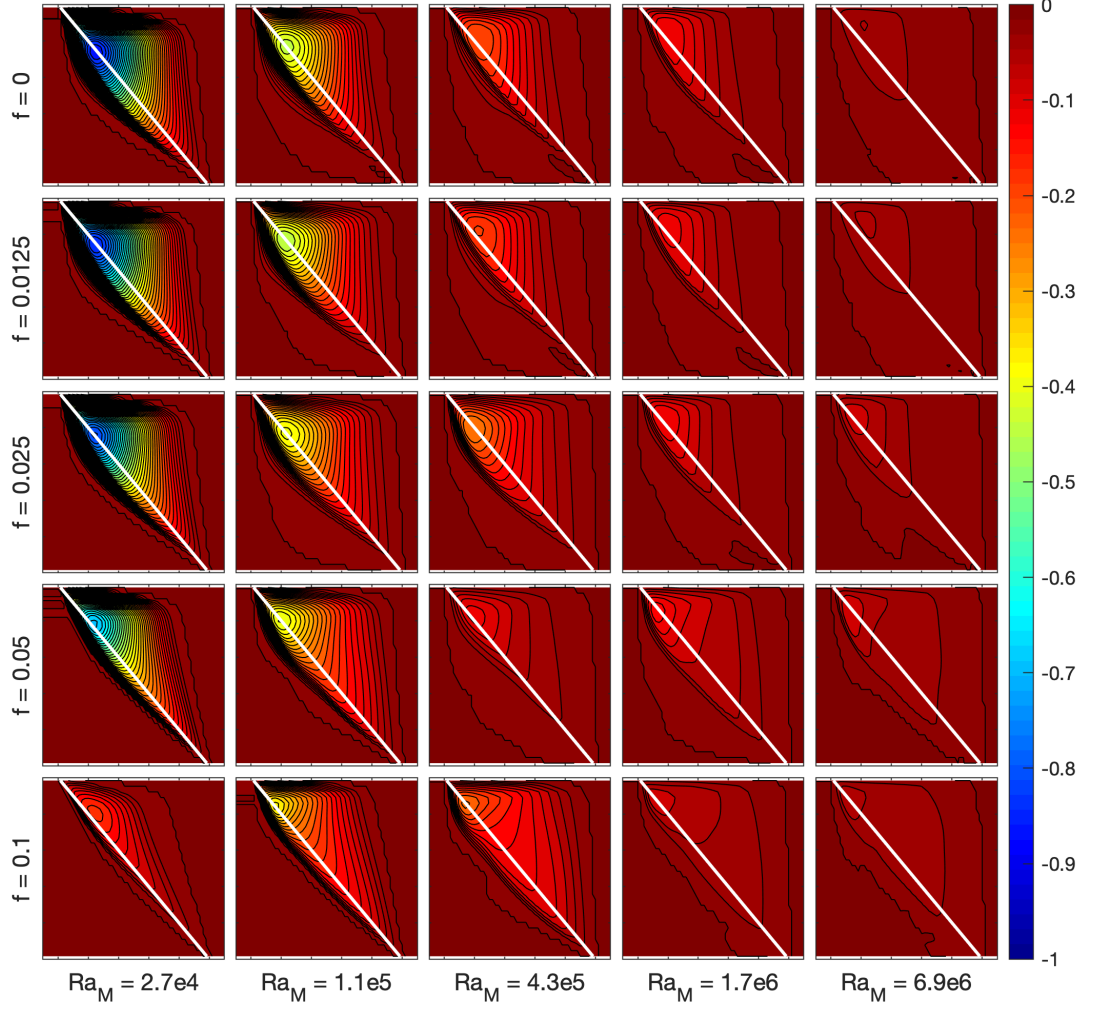
Figure 10. The time-averaged isentropic streamfunction for cases in $A = 20$. The momentum flux used for isentropic integration is scaled by velocity scale w_s.

Rotation has some impacts on the upward energy transport in our simulations, but it is much less significant than that of the Rayleigh number. To better assess the role of rotation here, we focus on assessing how the heat transport and overturning are affected by rotation for a constant value of Ra_M. On the one hand, for low Rayleigh number, the heat transport of vortices in category D decreases with the convective Rossby number. In particular, the minimum of the isentropic streamfunction of category D is larger than in the non-rotating case. The first column of Figure 10 shows an increase of minimum Ψ_M with the rotation rate, and the heat transport reduces. The vortices in category D are in geostrophic balance with both low convective Rossby number and moist Rayleigh number of category, so the vortices share the same characteristics with Taylor vortices. Taylor vortices show a quasi-two-dimensional structure, and the vertical mo-

tion is restricted, so the heat transport reduces. Despite the reduction in heat flux, the vortices in category D show the asymmetric of moist convection, and the trend of heat transport in category D agrees with the standard rorting Rayleigh-Bénard convection which the updraft and downdraft are symmetric, as shown in R. J. Stevens et al. (2013).

On the other hand, at larger Rayleigh number, convection in category TC shows an increase in overturning in the presence of rotation and with high moist Rayleigh number and the vortices receive additional heat transport from the Ekman layer to the eyewall. In Figure 10, the minimum of the isentropic streamfunction decreases with the rotation compared to the non-rotating cases. The Ekman layer provides extra vertical heat flux in the ascending updraft, and the heat transport of moist convection is dominated by the moist updraft, as shown in Figure 4. From the isentropic point of view, the formation of the eyewall separates the saturated updraft and unsaturated downdraft and prevents the mixing of two types of parcels, so the efficiency of heat transport increases. Despite the extra Nusselt transport in the category TC, the upper bound for heat transport of hurricane-like vortices remains bounded as proved in Pauluis and Schumacher (2011).

4.3 Dry stratification vs. moist instability

As discussed earlier, under conditional instability, the moist buoyancy decreases with height, with $M_H < M_0$, but the dry buoyancy increases, with $D_H > D_0$, so that the layer is unstable for saturated parcels originating near the lower boundary, but stable for unsaturated parcels. In this section, we explore the extent to which the ratio between the dry and moist buoyancy gradients affects the development of intense vortices. To do so, we perform a set of simulations, varying values of the dry stratification (D_H and Ra_D) while keeping the moist stratification (M_H and Ra_M) constant, with a moist Rayleigh number of $Ra_M = 6.9 \times 10^6$. We investigate here 5 different values of the dry Rayleigh number, with $-Ra_D = 0.75, 1.5, 3.0, 6.0,$ and $12.0 Ra_M$, with the case $Ra_D = -3 Ra_M$ corresponding to the simulations studied in the previous section. We also ensure that the quiescent equilibrium remains right at the saturation margin by imposing the Brunt-Väisälä frequency to be $N_s^2 = H^{-1}(D_H - M_H)$. Two sets of simulations are performed, one without rotation, and one for a rate of rotation of $f = 0.05$ in the $A = 20$ domain.

Figure 11 shows a snapshot of vertical integrated moist buoyancy. The convection exhibits similar characteristics to the simulations studied in section 4.1. In the absence of rotation (top row), the cases with weaker dry stratification ($Ra_D = -0.75 Ra_M$, $Ra_D = -1.5 Ra_M$ and $Ra_D = -3 Ra_M$) lead to self-aggregated quasi-equilibrium. Cases with strong dry stratification ($Ra_D = -6 Ra_M$ and $Ra_D = -12 Ra_M$) only exhibit intermittent convection. For the rotating cases, all the cases reach the quasi-steady equilibrium and form the hurricane-like vortices as discussed in previous sections, but the number of vortices decreases as stratification increases.

In the rotating case, the Rossby deformation radius $L_R = f_0^{-1/2} D_H^{1/2}$ can be viewed as a characteristic scale for horizontal motion that increases as the stratification increases. In Figure 12, we show the Eulerian streamfunction (Equation 20) for the five experiments with rotation. The Eulerian streamfunction here is obtained by azimuthal averaging of the flow centered on the most intense vortex in the domain. It exhibits a general pattern similar to the cases in Figure 8, with a low level inflow, deep ascent near the storm center, upper level outflow and large-scale subsidence trough a large region away from the center. Of particular interest here is that diameter of the subsidence region appears to scale as the Rossby radius $L_R \sim D_H^{1/2}$. Despite these substantial changes in vortex size, tangential winds remain the same order of magnitude.

In the three cases with the strongest dry stratification ($Ra_D/Ra_M = -12, -6$ and -3), there is only one vortex within the domain, so we can reasonably assume that the
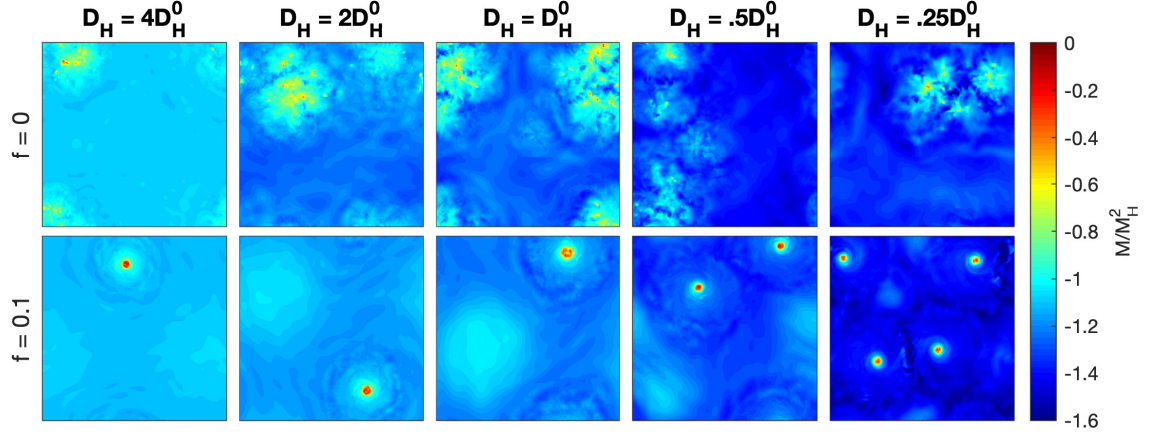
Figure 11. The instantaneous vertical integrated moist buoyancy for the non-rotating cases (upper panels) and the rotating cases (lower panels). The snapshots are selected in the recharged phase.

domain size, rather than the internal dynamics, is constraining the storm size. In these domain-constrained cases, increasing stratification cannot result in an increase in storm size, but it does appear to reduce the strength of the secondary circulation, as indicated by the magnitude of the Eulerian streamfunction in Figure 12. In contrast, when the stratification is weak enough ($Ra_D/Ra_M = -1.5$ and -0.75), multiple storms are present. The magnitude of the Eulerian streamfunction however is roughly unaffected, implying that the mass overturning associated with each vortex remains approximately the same. However, as the number of vortices increases when the stratification decreases, the overturning mass transport will similarly increase.

In Figure 13, the probability distribution function shows the asymmetry of moist convection. The bulk of the distribution is unsaturated but the area covered by saturated parcels increases as the dry stratification is reduced. In the presence of rotation, we observe a secondary maximum in the PDF at high values of the moist buoyancy that indicates the presence of a warm core. The area covered by the warm core increases as the dry stratification is reduced, consistent with the presence of more vortices in these simulations.

Figure 14 shows the isentropic streamfucntion. The scaling for the streamfunction (Equation 24) can be rewritten as

$$\Delta\Psi \approx \left(1 - \frac{Ra_M}{Ra_D}\right)\kappa, \tag{25}$$

after taking advantage of the fact that $\frac{N_s^2 H}{D_H} = \left(1 - \frac{Ra_M}{Ra_D}\right)$ for the Kuo-Bretherton case. This implies a strong increase in the atmospheric overturning as the dry stratification decreases as seen in Figure 14. Overall, the rotating and non-rotating cases exhibit similar sensitivity to dry stratification. As noted before, the rotating case exhibits ascent of parcels with very high moist buoyancy, consistent with saturated ascent of the intense vortices within the eyewall, while the streamfunction for the non-rotating cases indicates the presence of deep convective downdrafts that bring parcels with low moist buoyancy close to the lower boundary.
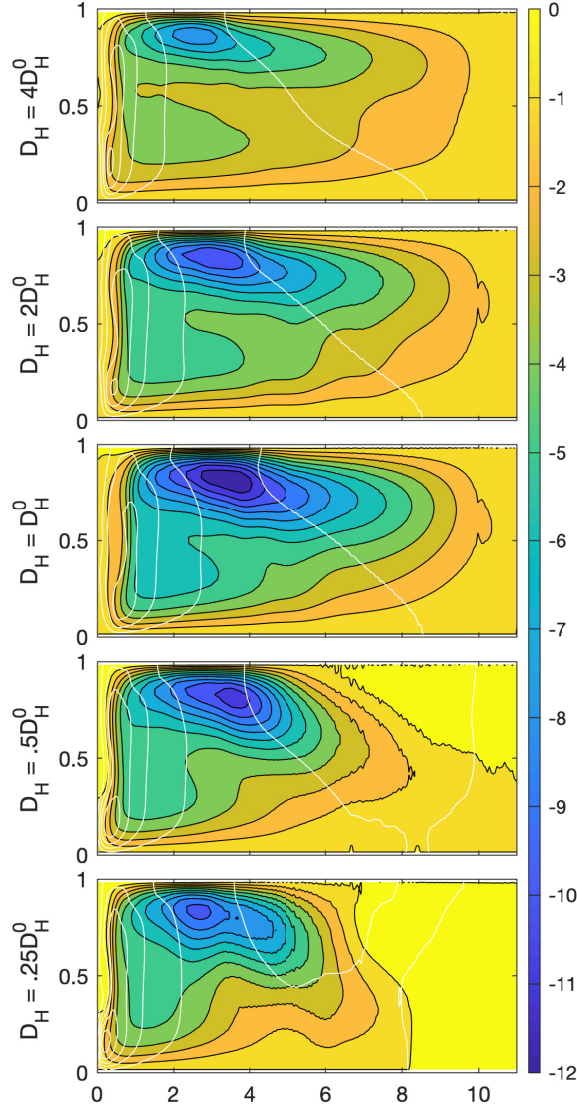
Figure 12. The time-averaged Eulerian streamfunction as in Figure 8 but with different dry Rayleigh number.

5 Conclusions

In this study, we investigate the impact of rotation on moist convection in a conditionally unstable atmosphere. We simulate a Boussinesq atmosphere with simplified thermodynamics for phase transitions forced by prescribing the temperature and humidity at the upper and lower boundaries. While highly idealized, this system exhibits many similarities with atmospheric convection. Furthermore, it can be fully described by only six non-dimensional numbers, including moist and dry Rayleigh number and convective Rossby number, which makes investigation of the parameter space more tractable. The governing equations are solved numerically using an adaptive mesh refinement, variable-density incompressible Navier-Stokes solver, IAMR to generate a set of over 30 simula-
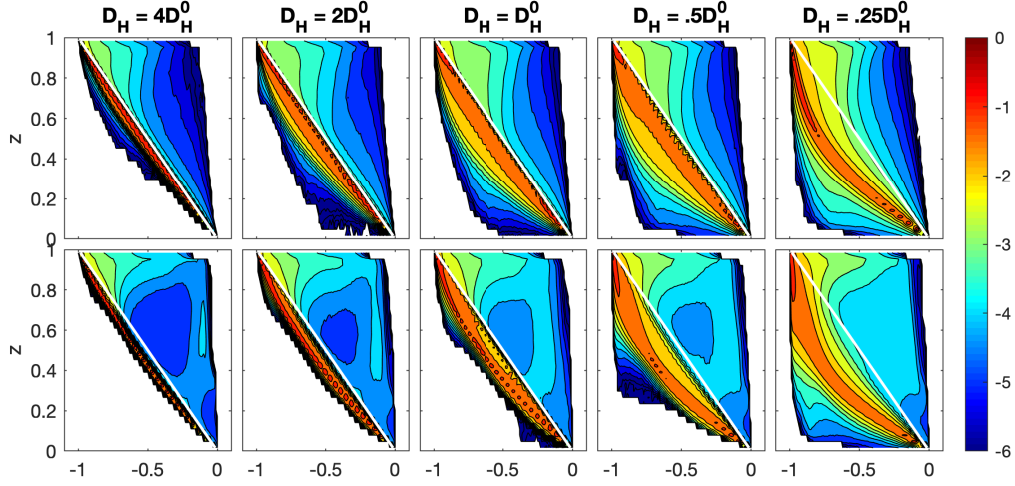
Figure 13. The time-averaged probability distribution function in the absence of rotation (upper panels) and in the presence of rotation (lower panels) for the different ratio of Ra_D to Ra_M in the Kuo-Bretherton regime.

tions of convection under different combinations of the dry and moist Rayleigh number and rotation.

In the absence of rotation, convection aggregates into active patches separated by unsaturated regions. In both rotation and non-rotation cases, the system exhibits an asymmetry typical of moist convection, with strong upward motions of moist saturated air parcels in a small portion of the domain, compensated by slow subsidence of mostly unsaturated air parcels over most of the domain. When rotation is included, the updrafts organize into intense hurricane-like cyclonic vortices surrounded by broad quiescent regions. This regime occurs when the time scale for rotation is about ten times longer the convective time-scale. The intense vortices observed in our simulations exhibit many of the characteristics of tropical cyclones: a warm, moist vortex core with the strongest azimuthal wind near the lower boundary, a strong secondary circulation characterized by low level inflow, ascent in a circular eyewall and upper level outflow. The vortex structure is consistent with theoretical models for tropical cyclones, include the role of slantwise convection in the eyewall (Emanuel, 1986). A key finding here is that the emergence of intense vortices in our simulations indicates that tropical cyclogenesis may occur even in the absence of interactions with radiation, surface flux feedback, or reevaporation of precipitation, as all these processes are omitted from our simulation. Rather, our results indicate that the formation and maintenance of hurricane-like vortices involve a combination of rotation and thermodynamic forcing in a conditionally unstable atmosphere.

We categorize three equilibrium states based on the exploration of parameter space of moist convection in the conditionally unstable layer. The exploration suggests that to form the hurricane-like vortices requires marginal rotation with sufficient moist Rayleigh number. When the rotation is irrelevant, the convection aggregates into patches, and the size of self-aggregated convection increases with the moist Rayleigh number. With the increase in moist Rayleigh number, the convection turns into intermittent convection. As the rotation becomes relevant, the large patches start to form the hurricane-like vortices, associated with secondary circulation characterized by an Ekman flow at the lower boundary. The Eulerian streamfunction indicates the radius of vortices increases with moist Rayleigh number and decreases with the rotation rate. In the dissipated vortices
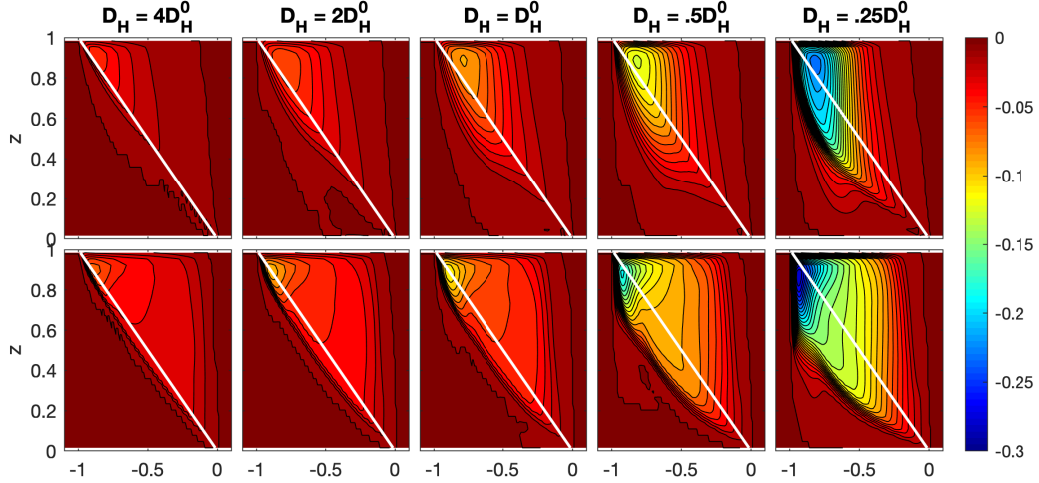
Figure 14. The time-averaged isentropic streamfunction (lower panels) as shown in Figure 6 in the absence of rotation (upper panels) and in the presence of rotation (lower panels) for the different ratio of Ra_D to Ra_M in the Kuo-Bretherton regime.

regime, as the rotation rate increases, the depth of the Ekman layer and the Ekman transport decrease. This reduction limits the vertical transport in the vortex, and the radius and the strength decrease rapidly.

We also investigate the atmospheric overturning by separating the ascending and descending motion in terms of their moist buoyancy, following the isentropic analysis method developed by Pauluis and Mrowiec (2013); Mrowiec et al. (2016). The overturning is characterized by a strong asymmetry between ascent of saturated air in intense updrafts stretching the entire column, and the slow descent of unsaturated air over most of the domain. In the presence of rotation, the area occupied by warm moist air increases significantly, indicating the presence of warm core structure for the undiluted ascent. In addition, when hurricane-like vortices are present, the total mass transport by the atmospheric overturning increases by about 20% by preventing mixing with low buoyancy parcels. This increase of atmospheric overturning also corresponds to an increase in the upward energy transport. This is consistent with previous findings on (dry) Rayleigh-Bénard convection R. J. Stevens et al. (2013) that have found an increase in the Nusselt number for intermediate values of the convective Rossby number in rotating convection.

Conditional instability occurs when the atmosphere is stable for unsaturated motions, but unstable for saturated parcels. In our idealized set up, this corresponds to a positive moist Rayleigh number and negative dry Rayleigh number. We have shown here that the atmospheric overturning is directly affected by the ratio between these two Rayleigh numbers. The rotating and non-rotating cases show similar sensitivity to the ratio. When the convection experiences less suppression from environment stability, the total mass transport increases to sustain more smaller vortices in the domain. In contrast, the limited mass transport can only sustain a single vortex if the convection is suppressed by the environmental stability.

Our result shows that a combination of conditional instability and rotation is sufficient to the formation of hurricane-like vortices in our idealized setting. As these conditions are present through most of the tropical atmosphere, this raise the question as to why tropical cyclones remain, thankfully, rare occurrences. The answer to this ques-

865 tions is likely in the processes that were omitted in our idealized simulations, such as ra-
866 diative transfer, cloud microphysics and variations in the lower boundary conditions (i.e.
867 the land-sea contrast, and variation in sea surface temperature). Further studies are nec-
868 essary to address these in greater detail and to more broadly investigate the rich range
869 of behavior exhibited by moist convection.

Appendix A Stability analysis of moist Rayleigh-Bénard convection

871 First, we provide the derivation of the dimensionless equations. The characteris-
872 tic scale of moist Rayleigh-Bénard convection is determined by unstable moist buoyancy,
873 denoted as $[B] = M_0 - M_H$. We can characterize the system by convective velocity
874 scale $w_s = \sqrt{H(M_0 - M_H)}$. The nondimensional version of the equation is obtained
875 by defining the nondimensional variables (with asterisks)

$$\mathbf{u}^* = [U_C]^{-1}\mathbf{u} \tag{A1}$$
$$(x^*, y^*, z^*) = H^{-1}(x, y, z) \tag{A2}$$
$$t^* = \frac{[U_C]}{H}t \tag{A3}$$
$$p^* = [U_C]^{-2}p' \tag{A4}$$
$$(B^*, D^*, M*) = [B]^{-1}(B, D, M). \tag{A5}$$

876 Note that we keep the mean profile in both dry and moist buoyancy, in contrast to Paulius
877 and Schumacher (2010) removing the mean profile.

878 The dimensionless version of equations together with the decomposition Equation
879 (A1) is

$$\frac{d\mathbf{u}^*}{dt} = -\nabla_* p^* + B^*(M^*, D^*, z^*) + \sqrt{\frac{Pr}{Ra_M}}\nabla_*^2\mathbf{u}^* \tag{A6}$$
$$\nabla_* \cdot \mathbf{u}^* = 0 \tag{A7}$$
$$\frac{dD*}{dt^*} = \frac{1}{\sqrt{PrRa_M}}\nabla_*^2 D'^* \tag{A8}$$
$$\frac{dM*}{dt^*} = \frac{1}{\sqrt{PrRa_M}}\nabla_*^2 M'^*. \tag{A9}$$

880 Here, $\frac{d}{dt^*} = \frac{\partial}{\partial t^*} + u^*\dot{\nabla}_*$ denotes the nondimensional version of the material derivative,
881 while $\dot{\nabla}_*$ and ∇_*^2 are the nondimensional gradient and Laplacian operators. These equa-
882 tions contains three nondimensional parameters. In this study, we keep the mean pro-
883 file of dry and moist buoyancy in the nondimensional equation. This selection make the
884 equations for buoyancy a homogeneous advection-diffusion equation, and Dirichlet bound-
885 ary conditions are applied to the top and bottom boundary.

886 The linear stability conditions typically depend on all five non-dimensional num-
887 bers. If both the dry and moist Rayleigh number are larger than the critical value $Ra_C =$
888 1.1×10^3, for our cases, then the flow is linearly unstable. Note that the critical Rayleigh
889 number depends on the boundary conditions. An interesting instability occurs however
890 when the moist Rayleigh number is supercritical, $Ra_M > Ra_C$, but the dry Rayleigh
891 number is negative - meaning that the dry buoyancy is stably stratified, corresponding
892 to a conditionally unstable layer. The linear stability conditions depends on the degree
893 of saturation in the layer as illustrated in Figure (1a).

894 In atmospheric science, it is common to define the potential for convective insta-
895 bility in terms of the convective available potential energy(CAPE) for the parcel rising
896 from the surface $z = 0$. In MRBC, we can define maximum intensity(MI) that is sim-
897 ilar to CAPE in atmosphere dynamics, and the convective velocity scale, w_s, is related
898 to the maximum intensity. The convection is able to sustain when MI is positive. MI is

given by

$$MI = \int_0^H B(D_0, M_0, z) - \overline{B}(D, M, z)\, dz, \tag{A10}$$

where $\overline{B}$ denotes the horizontal average at height z. The MI in the linear diffusive profile is equal to

$$MI = \frac{H}{2}\min(M_0 - M_H, N^2 z + D_0 - D_H). \tag{A11}$$

Furthermore, with $CW_H = 0$, this implies $M_H = D_N - N^2 z$ and $CAPE = \frac{H}{2}(M_0 - M_H)$ depending only moist buoyancy given at the top boundary. Equation A10 implies a close connection between the moist Rayleigh number Ra_M and MI.

In general, a positive MI is not sufficient to guarantee unstable convective motion. In particular, the quiescent equilibrium state is unsaturated, i.e.,

$$M(z) < D(z) - N_s^2 z, \tag{A12}$$

small perturbations cannot cause a transition to convection. This case is referred as sub-critical conditionally unstable equilibrium (Pauluis & Schumacher, 2011). In the absence of rotation, the majority of this regime reaches the quiescent equilibrium with an initial perturbation as found in Pauluis and Schumacher (2011).

In Fiugre 1b, the stable straitification is exactly at the onset of saturation, i.e.

$$M(z) = D(z) - N_s^2 z, \tag{A13}$$

or $CW_0 = CW_H = 0$. This equilibrium state is referred as the Kuo-Bretherton regime (Kuo, 1961; Bretherton, 1987; Almgren et al., 1998). In the absence of rotation, a small perturbation leads to the transition of steady convection. In the Kuo-Bretherton regime, the convective velocity scale $w_s = \sqrt{H(M_0 - M_H)}$ is the reference scale that is applied to the comparison in the result of this study.

When the dry stability Ra_D is less than in the Kuo-Bretherton case, the equilibrium contains liquid water content at the top boundary, i.e. $CW_H > 0$, referred as super-critical conditionally unstable equilibrium. Pauluis and Schumacher (2011) suggests that regimes satisfying $M_H \geq D_H - N_s^2 H$ always has the transition to moist convection. This implies the convection can either relies the potential energy given from the conditional instability or the linear instability. The decreasing of D_H provides additional MI for convection, but it reduces the barrier for convection to develop through the linear instability.

Appendix B IAMR Algorithm

In this appendix we briefly review the basic fractional step scheme used at each refinement level in IAMR. Here the subscript denotes the spatial index, so $U_{i,j,k}$ represents the velocity at index (i, j, k), and the superscript denotes the temporal index, so U^n represents the velocity at the nth timestep. In this algorithm, velocity and dry and moist buoyancy are defined at cell centers at integer times and are denoted $U_{i,j,k}^n$, $D_{i,j,k}^n$ and $M_{i,j,k}^n$, respectively. Pressure is specified at cell corners (nodes) and is staggered in time, denoted as $p_{i+\frac{1}{2},j+\frac{1}{2},k+\frac{1}{2}}^{n+\frac{1}{2}}$. In the first step at each level, IAMR uses an unsplit second-order upwind predictor–corrector scheme to solve the advection–diffusion Equation (3) and (4) for the updated dry and moist buoyancy, and computes a provisional velocity field from Equation (1) without strictly enforcing the divergence constraint on velocity. That is,

$$\frac{U^* - U^n}{\Delta t} = -[\nabla \cdot (UU)]^{n+\frac{1}{2}} + \left[-\nabla p^{n-\frac{1}{2}} + \frac{\nu}{2}(\Delta u^n + \Delta u^*) + B^{n+\frac{1}{2}}\right] \tag{B1}$$

$$\frac{D^{n+1} - D^n}{\Delta t} = -[\nabla \cdot (DU)]^{n+\frac{1}{2}} + \left[\frac{\kappa}{2}(\Delta D^n + \Delta D^{n+1})\right], \tag{B2}$$

where the right hand side of the velocity equation includes an explicit evaluation of the advection term, a semi-implicit representation of the viscous term, a lagged pressure gradient, and a time-averaged buoyancy forcing term. The equation for moist buoyancy is analogous to the equation for dry buoyancy. The buoyancy term B in Equation B1 applies Equation 5 and yields

$$B^{n+\frac{1}{2}} = \max\left(M^{n+\frac{1}{2}}, D^{n+\frac{1}{2}} - N_s^2 z\right), \tag{B3}$$

where $D^{n+\frac{1}{2}}$ is averaged by D^n and D^{n+1}, updated by Equation B2, and so for $M^{n+\frac{1}{2}}$.

In the second step, this intermediate field is projected onto the space of vector fields which approximately satisfy the divergence constraint (Almgren et al., 2000). A vector field decomposition is applied to $V = \left(\frac{U^* - U^n}{\Delta t}\right)$ to obtain the new velocity field U^{n+1}, and an update for pressure. See (Almgren et al., 1998) for more details about this algorithm.

Acknowledgments

References

Almgren, A. S., Bell, J. B., Colella, P., Howell, L. H., & Welcome, M. L. (1998, May). A Conservative Adaptive Projection Method for the Variable Density Incompressible Navier–Stokes Equations. *Journal of Computational Physics*, *142*(1), 1–46. doi: 10.1006/jcph.1998.5890

Almgren, A. S., Bell, J. B., & Crutchfield, W. Y. (2000, January). Approximate Projection Methods: Part I. Inviscid Analysis. *SIAM J. Sci. Comput.*, *22*(4), 1139–1159. doi: 10.1137/S1064827599357024

Bretherton, C. S. (1987). A Theory for Nonprecipitating Moist Convection between Two Parallel Plates. Part I: Thermodynamics and "Linear" Solutions. *Journal of the Atmospheric Sciences*, *44*(14), 1809–1827. doi: 10.1175/1520-0469(1987)044⟨1809:ATFNMC⟩2.0.CO;2

Bretherton, C. S. (1988). A Theory for Nonprecipitating Convection between Two Parallel Plates. Part II: Nonlinear Theory and Cloud Field Organization. *Journal of the Atmospheric Sciences*, *45*(17), 2391–2415. doi: 10.1175/1520-0469(1988)045⟨2391:ATFNCB⟩2.0.CO;2

Cronin, T. W., & Chavas, D. R. (2019, July). Dry and Semidry Tropical Cyclones. *Journal of the Atmospheric Sciences*, *2019*(1), 1–20. doi: 10.1175/JAS-D-18-0357.1

Emanuel, K. A. (1986, March). An Air-Sea Interaction Theory for Tropical Cyclones. Part I: Steady-State Maintenance. *Journal of the Atmospheric Sciences*, *43*(6), 585–605. doi: 10.1175/1520-0469(1986)043⟨0585:AASITF⟩2.0.CO;2

Khairoutdinov, M., & Emanuel, K. (2013, December). Rotating radiative-convective equilibrium simulated by a cloud-resolving model: ROTATING RCE. *J. Adv. Model. Earth Syst.*, *5*(4), 816–825. doi: 10.1002/2013MS000253

King, E. M., Stellmach, S., Noir, J., Hansen, U., & Aurnou, J. M. (2009, January). Boundary layer control of rotating convection systems. *Nature*, *457*(7227), 301–304. doi: 10.1038/nature07647

Kuo, H. L. (1961, November). Convection in Conditionally Unstable Atmosphere. *Tellus*, *13*(4), 441–459. doi: 10.1111/j.2153-3490.1961.tb00107.x

Mrowiec, A. A., Garner, S. T., & Pauluis, O. M. (2011, August). Axisymmetric Hurricane in a Dry Atmosphere: Theoretical Framework and Numerical Experiments. *Journal of the Atmospheric Sciences*, *68*(8), 1607–1619. Retrieved 2019-02-07, from `http://journals.ametsoc.org/doi/abs/10.1175/2011JAS3639.1` doi: 10.1175/2011JAS3639.1

Mrowiec, A. A., Pauluis, O. M., & Zhang, F. (2016, May). Isentropic Analysis of a Simulated Hurricane. *J. Atmos. Sci.*, *73*(5), 1857–1870. doi: 10.1175/JAS-D-15-0063.1

Muller, C. J., & Held, I. M. (2012, August). Detailed Investigation of the Self-Aggregation of Convection in Cloud-Resolving Simulations. *Journal of the Atmospheric Sciences*, *69*(8), 2551–2565. doi: 10.1175/JAS-D-11-0257.1

Pauluis, O. M., & Mrowiec, A. A. (2013, November). Isentropic Analysis of Convective Motions. *Journal of the Atmospheric Sciences*, *70*(11), 3673–3688. doi: 10.1175/JAS-D-12-0205.1

Pauluis, O. M., & Schumacher, J. (2010). Idealized moist Rayleigh-Benard convection with piecewise linear equation of state. *Communications in Mathematical Sciences*, *8*(1), 295–319. doi: 10.4310/CMS.2010.v8.n1.a15

Pauluis, O. M., & Schumacher, J. (2011, August). Self-aggregation of clouds in conditionally unstable moist convection. *Proceedings of the National Academy of Sciences*, *108*(31), 12623–12628. doi: 10.1073/pnas.1102339108

Pauluis, O. M., & Schumacher, J. (2013, April). Radiation Impacts on Conditionally Unstable Moist Convection. *J. Atmos. Sci.*, *70*(4), 1187–1203. doi: 10.1175/JAS-D-12-0127.1

Pauluis, O. M., & Zhang, F. (2017, October). Reconstruction of Thermodynamic Cycles in a High-Resolution Simulation of a Hurricane. *J. Atmos. Sci.*, *74*(10), 3367–3381. doi: 10.1175/JAS-D-16-0353.1

Schumacher, J., & Pauluis, O. M. (2010, April). Buoyancy statistics in moist turbulent Rayleigh–Bénard convection. *J. Fluid Mech.*, *648*, 509–519. doi: 10.1017/S0022112010000030

Stevens, B. (2005, May). Atmospheric Moist Convection. *Annu. Rev. Earth Planet. Sci.*, *33*(1), 605–643. doi: 10.1146/annurev.earth.33.092203.122658

Stevens, R. J., Clercx, H. J., & Lohse, D. (2013, July). Heat transport and flow structure in rotating Rayleigh–Bénard convection. *European Journal of Mechanics - B/Fluids*, *40*, 41–49. doi: 10.1016/j.euromechflu.2013.01.004

Stevens, R. J. A. M., Zhong, J.-Q., Clercx, H. J. H., Ahlers, G., & Lohse, D. (2009, July). Transitions between Turbulent States in Rotating Rayleigh-Bénard Convection. *Phys. Rev. Lett.*, *103*(2), 024503. doi: 10.1103/PhysRevLett.103.024503

Stull, R. B. (Ed.). (1988). *An Introduction to Boundary Layer Meteorology*. Dordrecht: Springer Netherlands. doi: 10.1007/978-94-009-3027-8

Weidauer, T., Pauluis, O. M., & Schumacher, J. (2010, October). Cloud patterns and mixing properties in shallow moist Rayleigh–Bénard convection. *New Journal of Physics*, *12*(10), 105002. doi: 10.1088/1367-2630/12/10/105002

Weidauer, T., Pauluis, O. M., & Schumacher, J. (2011, October). Rayleigh-Bénard convection with phase changes in a Galerkin model. *Phys. Rev. E*, *84*(4), 046303. doi: 10.1103/PhysRevE.84.046303

Wing, A. A., Camargo, S. J., & Sobel, A. H. (2016, July). Role of Radiative–Convective Feedbacks in Spontaneous Tropical Cyclogenesis in Idealized Numerical Simulations. *J. Atmos. Sci.*, *73*(7), 2633–2642. doi: 10.1175/JAS-D-15-0380.1

Wing, A. A., Emanuel, K., Holloway, C. E., & Muller, C. (2017, November). Convective Self-Aggregation in Numerical Simulations: A Review. *Surv Geophys*, *38*(6), 1173–1197. doi: 10.1007/s10712-017-9408-4

Zhang, W., Myers, A., Gott, K., Almgren, A., & Bell, J. (2021, June). AMReX: Block-structured adaptive mesh refinement for multiphysics applications. *The International Journal of High Performance Computing Applications*, 109434202110228. Retrieved 2021-07-21, from `http://journals.sagepub.com/doi/10.1177/10943420211022811` doi: 10.1177/10943420211022811

Zhong, J.-Q., & Ahlers, G. (2010, December). Heat transport and the large-scale circulation in rotating turbulent Rayleigh–Bénard convection. *J. Fluid Mech.*, *665*, 300–333. doi: 10.1017/S002211201000399X